Particuology 115 (2026) 91–105

Contents lists available at ScienceDirect

Particuology

journal homepage: www.elsevier.com/locate/partic

# Fine-tuning particle coatings: A comparative study of liquid atomization methods in fluidized bed processes

Serap Akbas[a,*], Maksim Mezhericher[b], Torsten Hoffmann[a], Nikolay Razorenov[c], Zehao Pan[b], Evangelos Tsotsas[a]

[a] Thermal Process Engineering, Otto von Guericke University, Universitätsplatz 2, 39106, Magdeburg, Germany
[b] Mechanical and Aerospace Engineering, Princeton University, Princeton, NJ, 08544, USA
[c] Mechanical Engineering, Shamoon College of Engineering, Beer Sheva, 84100, Israel

## HIGHLIGHTS

- A newly developed three-channel coaxial nozzle was applied in fluidized bed particle coating.
- The new nozzle generates droplets ~10 μm, bridging the gap between aerosol generators and conventional nozzles.
- Non-porous glass and porous γ-$Al_2O_3$ particles were coated using an aqueous sodium benzoate solution.
- Process yield, coating coverage, coating thickness, and surface roughness were evaluated.
- The new nozzle shows strong potential as an alternative to conventional nozzles by producing finer droplets.

## GRAPHICAL ABSTRACT

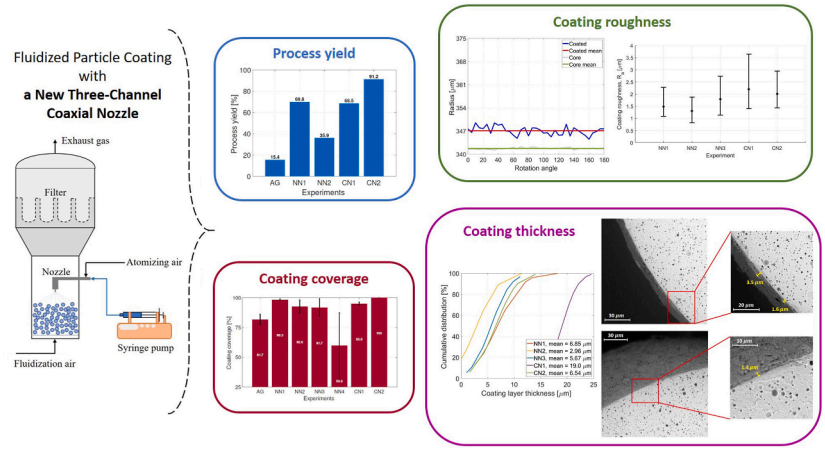


## ARTICLE INFO

*Keywords:*
Fluidized bed
Coating particles
Atomization
Process yield
Coverage
Layer thickness
Coating surface roughness

## ABSTRACT

This study compares the performance of a new three-channel coaxial nozzle with a conventional Schlick nozzle in fluidized bed particle coating. The new nozzle produces droplets with a Sauter mean diameter of around 10 μm, offering a middle ground between aerosol and conventional nozzles. Yields of processes, coating coverages of particles, coating thickness and surface roughness were compared for the same experimental conditions of these nozzles. Non-porous glass particles (mean diameter 653 μm) and porous γ-$Al_2O_3$ particles (mean diameter 610 μm) were used as cores, with an aqueous sodium benzoate (NaB) solution as the coating liquid. A scanning electron microscope (SEM) was utilized to capture images of the particles after each experiment. To analyze the coverage on the particle surfaces, MATLAB image processing was applied to SEM images of coated particles. Moreover, these images were used to determine the surface roughness of the coating. In addition to manual measurements of coating thickness on particles by image processing, some coated γ-$Al_2O_3$ particles were sectioned to measure the coating thickness by ImageJ. The manual thickness measurements were supplemented

* Corresponding author.
*E-mail address:* serap.akbas@ovgu.de (S. Akbas).

https://doi.org/10.1016/j.partic.2026.05.008
Received 17 July 2025; Received in revised form 27 April 2026; Accepted 12 May 2026
Available online 21 May 2026

by results obtained by laser scattering. The coating process by means of the new nozzle was also compared with an aerosol coating process which has droplet size with a mean diameter of around 1 μm, in terms of process yield, product coating coverage and thickness. The new nozzle acts as an intermediate between the aerosol generator and the conventional Schlick nozzle in terms of droplet size. These findings suggest that the new nozzle has significant potential for use in fluidized particle coating, as an alternative to conventional nozzle, offering smaller droplet size.

## 1. Introduction

For many industrial applications, the process of coating particles has importance. Some of the industrial purposes can be listed as battery material stabilization, active ingredient release control for drugs, encapsulation of catalysts, taste/odor masking, adding protective layers to seeds in agricultural industry, etc. (Bérengère Guignon & Dumoulin, 2002; Capece & Dave, 2011; Culver et al., 2019; Kleinbach & Riede, 1995; Turton et al., 1999; Wan & Lai, 1991; Werner et al., 2007; Zuo et al., 2023). Particle coating in conventional spray fluidized beds (SFB) is an established industrial process that is continuously being enhanced through the growing availability of advanced mathematical models and experimental techniques (Kieckhefen et al., 2019; Pietsch et al., 2019; Rieck et al., 2016, 2020; Sondej et al., 2016). However, the coating layers provided by SFB are generally coarsely structured and thick (in the range of 20 to 150 μm, with a typical mean droplet size of 40 μm) (Akbas et al., 2023, 2024; Tsotsas, 2012). Therefore, existing SFB technologies are inadequate for producing particles with ultrathin, high-resolution coatings required for several industries such as chemical, pharmaceutical, biochemical, and biomedical (Mezhericher et al., 2020). For smaller droplet size (as well as to reduce the coating thickness at full coverage), alternative atomizers exist like piezoelectric, ink-jet printing nozzles, but they are constrained by their limited capacity to handle large throughputs of high solid content liquids (Akbas et al., 2023). To address this, a new three-channel coaxial nozzle developed at Princeton University was tested, capable of producing smaller droplets.

With the purpose of producing ultrathin and high-resolution coating, Mezhericher et al. (2020) proposed a transition from conventional spray to aerosol fluidized bed (AFB) coating using aerosol droplets. In that study, a new aerosol generator (with a mean droplet diameter of around 1 μm) by Mezhericher et al. (2017, 2019) was used. The coating thickness with sodium benzoate (NaB) was measured as 2.7 μm on the surface of $\gamma$-$Al_2O_3$ particles (with a mean diameter of 638 μm) at the end of 1 h coating time. The same aerosol generator was later used in the study of Akbas et al. (2023) to investigate island growth on fluidized particle surfaces (in early-coating stage) as a result of preferential deposition of aerosol droplets on already occupied spots on the particle surface. In that study, the particles were not yet fully covered at the end of 1 h process time. Process conditions' impact on aerosol coating coverage and process yield was investigated in detail in the study of Akbas et al. (2024) by performing AFB experiments and comparing results with Monte Carlo simulations. Additionally, those authors increased the process time until 6 h to obtain fully covered particles by aerosol droplets. After 3 h, $\gamma$-$Al_2O_3$ particles were fully covered. Coating thickness was found to range from 0.7 to 2.8 μm in SEM pictures of cut $\gamma$-$Al_2O_3$ particle after 3 h process time; after 6 h process time, it was measured to range from 1.5 to 6.4 μm.

There is a gap between the coating thickness obtained by using aerosol droplets when full coverage is attained (around 1 μm (Akbas et al., 2024)) and coating thickness provided by a conventional nozzle (in literature, ranging from 20 to 150 μm (Akbas et al., 2023; Akbas et al., 2024; Tsotsas, 2012)). As in the study of Akbas et al. (2024), it is possible to get thicker coatings also with the aerosol generator, by simply performing the coating process longer. However, it is time consuming (around 6 μm coating thickness after 6 h of process time) because of the smallness of the aerosol droplets as well as the lower process yield compared to two-fluid nozzle processes. Therefore, in the current study, the main aim was to fill the gap between coating layers using aerosol droplets and using spray provided by a conventional nozzle, by performing coating experiments with a newly developed three-channel coaxial nozzle from Princeton University. The new nozzle creates droplets with a Sauter mean diameter of around 10 μm (for the specific experimental conditions in this study) that is indeed bigger than aerosol droplets (typically Sauter mean diameter of 1 μm) and smaller than the droplets from a conventional Schlick nozzle also used in this study with Sauter mean diameter of 20 μm (typically, mean diameters of around 40 μm are reported in literature for conventional nozzles (Akbas et al., 2023; Akbas et al., 2024; Tsotsas, 2012)).

For a same process yield and same amount of sprayed coating solids, population-averaged coating thickness remains constant, regardless of spray droplet size. However, the coating thickness when full coverage is reached is greatly influenced by droplet size, as the time required to achieve full coverage depends on the droplet footprint area. Droplet size also impacts coating surface roughness, or the intra-variability of coating thickness. Smaller droplets result in lower surface roughness, as they form building blocks (BB) of smaller height after drying of deposited droplets. In contrast, larger droplets are more likely to create larger voids between building blocks during droplet deposition, increasing both the average porosity and surface roughness of the coating layer. Consequently, the new nozzle is expected to produce a thinner and smoother coating layer when the full coverage is reached compared to conventional nozzles. The new nozzle was also expected to achieve a higher process yield compared to the aerosol generator. The primary reason for the reduced yield in the aerosol generator process was the premature drying of small aerosol droplets before they could deposit on the particles (Akbas et al., 2023). This effect can be reduced by producing larger droplets with the new nozzle, which may lead to an improved coating process yield.

Firstly, the experimental setup for different atomization methods (the aerosol generator, the new nozzle, and the conventional nozzle), the experimental plan, and post-processing steps are explained in the following paper. Subsequently, process yields and coating coverages provided by these three atomization methods are compared, and coating structures are evaluated. Finally, coating thicknesses of particles from different experimental conditions are manually obtained and compared, additionally supported by laser scattering measurements.

The use of the new nozzle has been previously proven for spray drying of pharmaceutics (Poozesh et al., 2024). The present study is intended as a proof-of-concept to evaluate the feasibility and coating performance of this newly developed three-channel coaxial nozzle for fluidized bed particle coating applications. The main objective is to understand how droplet size affects coating properties under controlled experimental conditions, rather than to perform a full aerodynamic nozzle characterization or design optimization. The results provide a first step toward developing a more detailed and comparative investigation in future work.

## 2. Experimental setup, materials and characterization

### 2.1. Fluidized bed setup

All the coating experiments and post processing analysis were performed at Otto von Guericke University. A laboratory-scale fluidized bed (GPCG 1.1, Glatt Ingenieurtechnik GmbH, Weimar, Germany), which is

the same bed as in the studies of Akbas et al. (2023, 2024), was used for the coating processes in this study. The cylindrical fluidization chamber (plexiglass, with access windows at the side for the experiments with aerosol generator) was changed to another plexiglass chamber of same size without windows. It has an inner diameter of 150 mm and height of 450 mm. The mean pore size of the sintered metal gas distributor plate is 100 μm.

### 2.1.1. Atomization methods

In this study, to atomize the coating solution, two different nozzles were used: the new nozzle, which was recently developed, and a conventional two-fluid nozzle (Düsen Schlick GmbH, type: 970/0 S4, with an orifice diameter of 0.8 mm). The new three-channel coaxial nozzle was developed at Princeton University and is commercialized by Inaedis, Inc. Due to intellectual property considerations, detailed geometric specifications (e.g., internal dimensions, orifice geometry) are not disclosed in this publication. However, the nozzle is characterized in this study by its operating conditions and resulting performance. In operation, it is mounted centrally in the fluidized bed analogous to the conventional nozzle. While the external connections are similar to standard industrial two-fluid nozzles, the internal geometry is designed to generate fine droplets (Sauter mean diameter ~10 μm) at low liquid flow rates without the clogging often associated with conventional nozzles operated in this regime. The working principle of the new nozzle is based on the atomization of a thin liquid film by bilateral gas shear, as described in the recently published international patent application (Mezhericher et al., 2025). Unlike conventional two-fluid nozzles (including the Schlick nozzle used in this study) where liquid exits through a central orifice and is sheared by a surrounding gas flow from one side only, the new nozzle employs a three-channel coaxial architecture. Liquid is fed through a middle annular channel, forming a thin film, while gas flows simultaneously through both an inner channel and an outer annular channel. This bilateral gas shear acts on both surfaces of the thin liquid film, disintegrating it into fine droplets. The relevant aerodynamic Weber number for this geometry is $\mathrm{We} = \rho_g v_{rel}^2 \delta/\sigma_l$, where $\delta$ is the characteristic thickness of the liquid film, $v_{rel}$ is the relative gas-liquid velocity, $\rho_g$ is the gas density, and $\sigma_l$ is the liquid surface tension. Because the liquid is pre-formed into a thin annular film, the characteristic length $\delta$ is inherently smaller than the orifice diameter of a conventional two-fluid nozzle. Since droplet diameter scales with film thickness (thinner films produce smaller ligaments and consequently smaller droplets), this geometry directly yields finer atomization at comparable operating pressures. Combined with bilateral shear enhancing breakup efficiency, the new nozzle produces Sauter mean diameters of approximately 10 μm (Fig. 2) compared to approximately 20 μm for the Schlick nozzle under the same operating conditions. The underlying atomization physics of thin liquid film disintegration by gas jets was originally demonstrated by Mezhericher et al. (2017), further characterized using a semi-empirical model by Mezhericher et al. (2019), and theoretically formalized (including atomization diagrams based on first principles) by Mezhericher & Stone (2022). Previously, in the study of Poozesh et al. (2024), the new nozzle of the current study was used as an atomizer in the laboratory-scale prototype of the novel Rapid Room-Temperature Aerosol Drying (RTAD) technique for the production of biopharmaceuticals. Here, in the current study, the same innovative two-fluid nozzle is used to produce droplets to coat particles inside of a fluidized bed. The droplet production mechanism is not the main focus of this study, but the resulting performance in fluidized bed particle coating processes.

Fig. 1 shows the experimental setup used either with the new or with the conventional Schlick nozzle to atomize the coating liquid.

For the fluidized bed coating experiments, the new nozzle and the conventional Schlick nozzle were located at the center of the fluidized chamber with same height (15 cm) from the distributor plate. Although Fig. 1 schematically illustrates a top-spray configuration in which the nozzle appears isolated from the bed for clarity, the actual fluidized bed exhibits complex heterogeneous particle motion, including bubble formation and bubble bursting. As a result of these hydrodynamic fluctuations, particles intermittently reach the nozzle region during operations. A syringe pump was used to feed the coating solution to the nozzles with stable and constant volume flow rate. The maximum capacity of the used syringe was 60 mL, the largest available option.

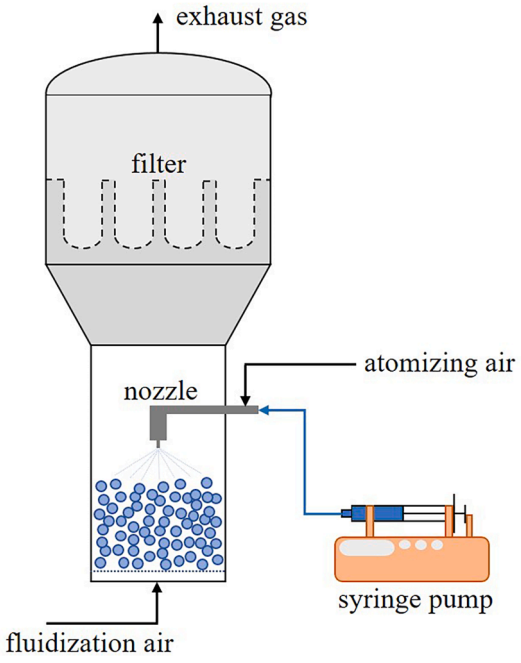


**Fig. 1.** Experimental setup for the experiments with new nozzle and conventional nozzle.

After having been filled with core particles, the process chamber was closed and fluidization air flow started. After the stabilization of fluidization air temperature, the coating solution was provided (by the syringe pump) to the nozzle in the upper side of the fluidization chamber. The experiment was completed when the total amount of coating solution in the syringe (60 mL) had been sprayed to the fluidized particles. Continuation of the coating process by refilling the syringe would require a pause in the process, which could lead to drying of the coating solution in the new nozzle and consequently block the nozzle tip due to its sensitive structure. To avoid this issue, experiments were conducted up to the total solution capacity of the syringe, without pausing the process for refilling. Additionally, to prevent crystallization of the coating material inside the nozzle and protect the nozzle, deionized water (60 mL) was sprayed through the nozzle at the end of each experiment for internal cleaning. This washing step was performed after removing the coated product from the fluidized bed.

The droplet size distributions produced by the new nozzle were characterized at Princeton University using a laser diffraction system (Spraytec, Malvern Instruments, 2015). Measurements were conducted at the same solution flow rates and atomizing pressures used for the experiments at Otto von Guericke University (explained later in Section 2.2). The system is equipped with a 5 mW Helium-Neon laser emitting at a wavelength of 632.8 nm with a beam diameter of 10 mm. The Malvern Spraytec device has a nominal measurement accuracy of better than ±1% for the median droplet diameter. Its performance was verified by the manufacturer using reference droplet sizes of 1 μm and 9 μm, showing measurement errors of less than ±0.3%. To minimize the influence of background light on measurement accuracy, all measurements were conducted in a dark room. Additionally, to eliminate the "beam steering" effect (an incorrect interpretation of scattered light signals due to refractive index gradients in the gas phase) the

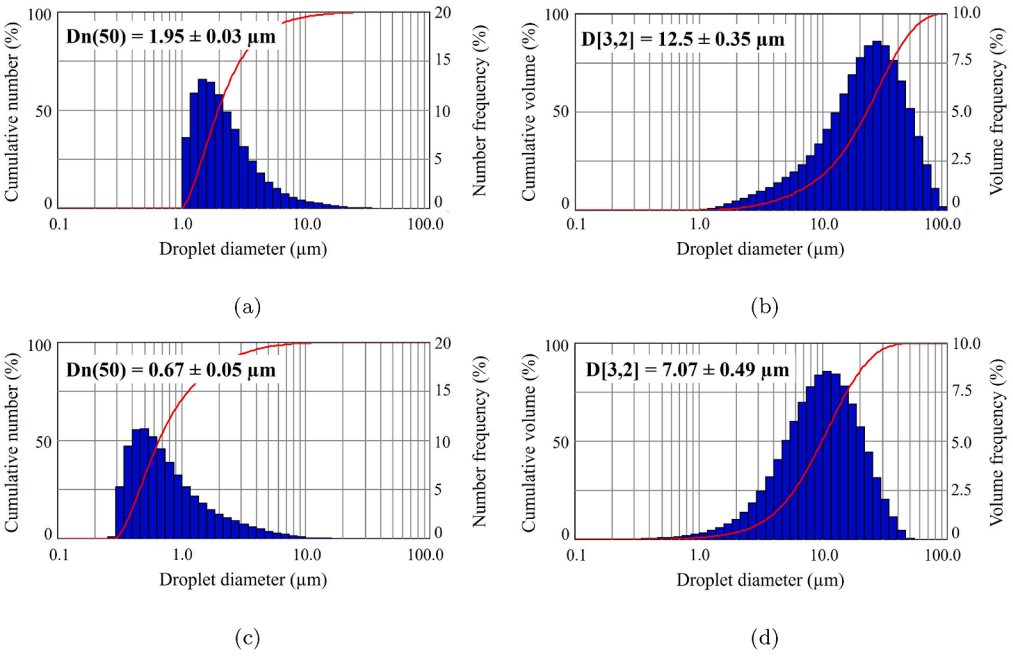


**Fig. 2.** Characterization of droplet diameters generated by the new nozzle. (a) Number-based and (b) volume-based size distributions of droplets produced at solution flow rate of 1.3 mL/min and atomization pressure of 1.5 (gauge) bar. (c) Number-based and (d) volume-based size distributions of droplets produced at solution flow rate of 8.5 mL/min and atomization pressure of 4 (gauge) bar. The corresponding number median diameters (Dn(50)) and Sauter mean diameters (D[3, 2]) are indicated. All data were measured for 30 wt% aqueous sodium benzoate solutions.

recommended procedures from the Malvern Spraytec manufacturer and relevant literature (Dumouchel et al., 2009; Liu et al., 2012; Sivakumar et al., 2015; Zhang et al., 2011) were followed. The spray was generated for 1–3 min under quasi-steady state conditions for each run of droplet size distribution measurement. The laser beam was positioned perpendicular to the droplet flow, and measurements were conducted at the nozzle outlet.

Number-based and volume-based droplet size distributions obtained with the new nozzle for the respective experimental conditions, together with the corresponding number median diameter, Dn(50), and Sauter mean diameter, D[3, 2], are shown in Fig. 2.

The Sauter mean diameter (D[3, 2]) was determined to be 12.5 µm for a solution flow rate of 1.3 mL/min at an atomization pressure of 1.5 gauge bar, and 7.07 µm for a solution flow rate of 8.5 mL/min at 4 gauge bar atomization pressure. The number median (Dn(50), Fig. 2a,c) and the Sauter mean diameters (D[3, 2], Fig. 2b,d) of the droplets produced by the new nozzle decreased as atomization pressure increased. These values additionally vary with the liquid feed flow rate to the nozzle, which is though not the focus of this study. Similar trends have been reported by Mezhericher et al. (2017, 2019, 2020) in studies characterizing aerosol droplet behavior.

The Schlick nozzle can generate droplets ranging from 10 to 50 µm in size, depending on the experimental conditions. Manufacturer-provided data specific to the nozzle type and the experimental parameters of this study were used for reference. These manufacturer-provided measurements were conducted at a liquid flow rate of 1 L/h, the lowest tested rate. The reported Sauter mean diameters were approximately 22 µm and 12 µm at atomizing pressures of 1.5 and 4 gauge bar, respectively. In this study, the solution flow rates were lower than 1 L/h, which likely resulted in smaller droplet sizes compared to those provided by the manufacturer. This happens because, at lower flow rates, the atomizing air has a stronger effect on breaking up the liquid into droplets, leading to finer atomization. However, the smallest droplet size achievable with the Schlick nozzle is still limited to around 10 µm.

To compare the particles (products) coated by using droplets from the new nozzle and the conventional Schlick nozzle with particles coated by means of aerosol droplets, some experimental data from the study of Akbas et al. (2024) was used. In that study, aerosol droplets to coat particles were created by the aerosol generator by Mezhericher et al. (2017, 2018, 2019) (for the experimental setup see Fig. 3). The Sauter mean diameter of aerosol droplets generated under the specified experimental conditions (later in Table 1) was measured using laser diffraction (Spraytec, Malvern Instruments) and found to be approximately 1 µm (Akbas et al., 2024; Mezhericher et al., 2020).

The main part of the aerosol generator was an elastic polyvinyl chloride (PVC) tube (8 mm inner diameter, 12 mm outer diameter, 220 mm length, bent to a circle). The tube had in total 144 orifices (4 in a cross-section (equidistant), 36 perforated cross-sections).

The aerosol inlet was placed on the side of the fluidization chamber about 45 mm high from the air distributor plate, unlike the location of nozzles in this study.

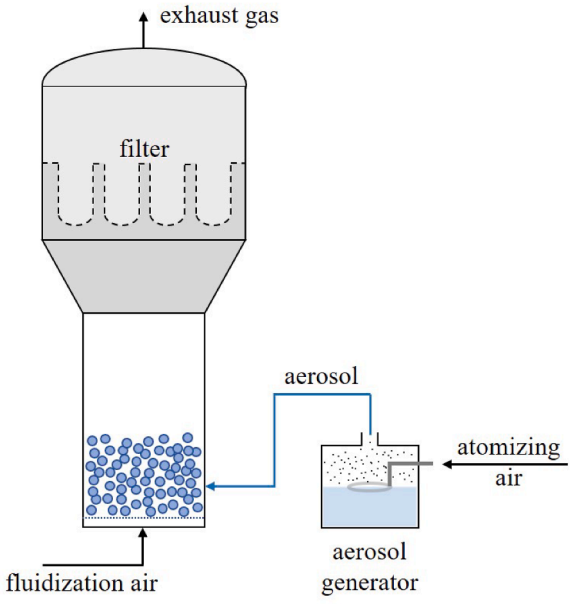


**Fig. 3.** Experimental setup with aerosol generator (Akbas et al., 2024).

**Table 1**
Experimental plan.

| Droplet production method | Experiment | Core material | Mass of core particles [g] | Volume flow rate of solution [mL/min] | Atomizing air pressure (gauge) [bar] | Fluidization air mass flow rate [kg/h] | Process time [min] | Sauter mean droplet diameter [$\mu$m] |
|---|---|---|---|---|---|---|---|---|
| **Aerosol generator** (Akbas et al., 2024) | **AG** | Glass | 1000 | 1.3 | 1.5 | 65 | 40 | 0.9 |
| **New nozzle** | **NN1** | Glass | 1000 | 1.3 | 1.5 | 50 | 46 | 12.5 |
| | **NN2** | Glass | 1000 | 8.5 | 4 | 50 | 7 | 7.07 |
| | **NN3** | $\gamma$-$Al_2O_3$ | 600 | 1.3 | 1.5 | 40 | 46 | 12.5 |
| | **NN4** | $\gamma$-$Al_2O_3$ | 600 | 8.5 | 4 | 40 | 7 | 7.07 |
| **Schlick nozzle** | **CN1** | Glass | 1000 | 1.3 | 1.5 | 50 | 46 | ~22 |
| | **CN2** | Glass | 1000 | 8.5 | 4 | 50 | 7 | ~12 |

#### 2.1.2. Core particles and coating solution

For the coating experiments, two different types of core materials were used in this study: spherical glass (soda lime) particles (Cerablast GmbH, Löchgau, Germany, same as in (Akbas et al., 2023, 2024)) and spherical porous $\gamma$-$Al_2O_3$ (Sasol GmbH, Hamburg, Germany, same as in (Akbas et al., 2024)). In (Akbas et al., 2024), it has been shown that washing the $\gamma$-$Al_2O_3$ particles with distilled water before performing a coating experiment has an affect on aerosol droplet deposition. Therefore, it needs to be noted that in the present study fresh (not washed) $\gamma$-$Al_2O_3$ particles were used for the experiments with the new nozzle.

The glass and $\gamma$-$Al_2O_3$ particles had mean diameters of 653 μm (measured with CAMSIZER in (Akbas et al., 2023)) and 610 μm (as supplied by the manufacturer), with respective densities of 2500 kg/m$^3$ and 1280 kg/m$^3$.

In literature, several studies have reported the use of sodium benzoate (NaB) solutions for particle coating, employing both conventional spray nozzles (Rieck et al., 2015; Sondej et al., 2016) and aerosol generators (Akbas et al., 2023, 2024; Mezhericher et al., 2020), as NaB adheres well to both porous and non-porous surfaces. In the study by Rieck et al. (2015), the simulated particle size distributions of NaB-coated particles obtained using a heat and mass transfer model showed good agreement with the experimentally measured data for both glass and $\gamma$-$Al_2O_3$ core particles. The structure of the NaB coatings on both glass and $\gamma$-$Al_2O_3$ particles is attributed to the crystallization of NaB during the drying process, where the resulting porosity can be influenced by the process parameters (Rieck et al., 2015; Sondej et al., 2015). Similar porous structures have also been reported for dried sessile NaB droplets on flat surfaces in the literature (Janocha & Tsotsas, 2022; Sondej et al., 2018). These findings indicate that the crystalline structure of such coatings on fluidized particles originates from the drying and crystallization behavior of NaB itself, rather than from mechanical breakage of smooth NaB layers during fluidization. Sodium benzoate possesses antibacterial properties and is commonly used as a preservative in the food industry, making it a coating material of practical industrial relevance. As described in Section 2.2, the experimental design of this study was based on our previous work involving aerosol droplet coating. In that earlier study (Akbas et al., 2024), it was showed that NaB solution can effectively coat particles without the use of any additional binder or polymer solution (such as HPMC or PVP), and that it adheres well to particle surfaces even when using droplets as small as 1 μm in diameter. For this reason, the NaB solution was retained in the present study to ensure a meaningful comparison with the previous aerosol coating results. Furthermore, the addition of a polymer would increase the risk of agglomeration (which we aimed to prevent) and could potentially cause damage to the newly developed nozzle. Therefore, a 30 wt% aqueous solution of sodium benzoate (NaB, $C_7H_5NaO_2$, Trigon Chemie GmbH, Schlüchtern, Germany) was utilized as coating liquid throughout all experiments.

### 2.2. Experimental plan

The starting point of the experimental plan was coating with the aerosol generator. For this, experiment E1 from Akbas et al. (2024) (which was in that study performed twice to check the reproducibility) was used as a reference. To this, fluidized particle coating processes using two different droplet production methods (the new nozzle and the conventional Schlick nozzle), two different volume flow rates of solution (1.3 and 8.5 mL/min), as well as different core materials (glass and $\gamma$-$Al_2O_3$) have been conducted. The operating parameters are listed in Table 1.

In the current study, the coating experiments were performed with 1000 g glass cores (same as in the study of Akbas et al. (2024)) but with 50 kg/h fluidization air mass flow rate (instead of 65 kg/h in (Akbas et al., 2024)). This adjustment was made to reduce particle transport toward the nozzle caused by bubble bursting, and thereby minimize particle-nozzle interactions that may lead to cluster formation due to localized over-wetting. Here, the term "over-wetting" refers to localized wetting near the nozzle tip rather than global bed over-wetting caused by insufficient drying. Particles entering the nozzle vicinity may be exposed to an intense spray and subsequently adhere to the nozzle tip after rapid solvent evaporation, promoting cluster formation. Such behavior is related to localized particle-nozzle interactions in the spray region and not to nozzle malfunction. Since the glass particles used in this study have a density of 2500 kg/m$^3$, whereas the $\gamma$-$Al_2O_3$ particles have a density of 1280 kg/m$^3$, if the same particle mass were used for both materials in a fluidized bed of identical dimensions, the $\gamma$-$Al_2O_3$ bed would contain approximately twice as many particles. This would result in a larger total surface area to be coated in the bed chamber. To ensure comparable coating conditions and a similar total particle surface area across experiments, the mass of $\gamma$-$Al_2O_3$ particles was therefore reduced to 600 g, instead of the 1000 g used for the glass particles. This adjustment also considers the slightly smaller mean particle diameter of the $\gamma$-$Al_2O_3$ particles (610 μm) relative to the glass particles (653 μm). The fluidization air flow rate was set to 40 kg/h for the $\gamma$-$Al_2O_3$ particles. This adjustment was implemented to minimize the risk of cluster formation and to ensure comparable bed heights for both particle types during the coating experiments. The fluidization air was supplied in a dry state. Its temperature was kept constant as 50 °C to ensure that all droplet sizes experienced the same evaporation flux. The expanded bed height was around 6 cm for all of seven experiments in Table 1.

Based on the saturation humidity at 50 °C, the dry fluidization air has a theoretical moisture removal capacity in the range of 0.40-3.74 kg of water under the operating conditions listed in Table 1. In contrast, approximately 0.046 kg of water is introduced through spraying of the 30 wt% NaB solution. This corresponds to only 1-11% of the moisture removal capacity of fluidization air. Even under the most demanding condition (NN4: highest spray rate and lowest fluidization air velocity), the process operated at approximately 11% of the saturation capacity. These results indicate that the experiments were conducted well below

the drying limit and that sufficient evaporation capacity was available throughout the experiments. For each experiment, the drying enthalpy can be calculated as $\dot{Q}_{dry} = \dot{m}_{air}\, c_p\, (T_{in} - T_{wb})$, where $T_{in} = 50\,^{\circ}C$ and $T_{wb}$ is the wet-bulb temperature of the fluidization air. The spray enthalpy requirement is $\dot{Q}_{spray} = \dot{m}_{water}\, \Delta H_{vap}$. The ratio $\dot{Q}_{dry}/\dot{Q}_{spray} \gg 1$ for all experiments, confirming that the process is globally energy-balanced. The spray rates and the drying capacity ratios of the experiments are listed in Table 2.

The minimum fluidization velocities were 0.728 and 0.583 m/s for the experiments with glass and $\gamma$-$Al_2O_3$ particles, respectively. Considering that the entrainment velocities of such small droplets are lower than the respective fluidization velocities, one may expect the droplets to be entirely carried out of the chamber and captured by the filters without depositing on the particle surfaces, leading to an unsuccessful coating process. However, the droplet deposition mechanism inside a fluidized chamber is complex. Deposition of droplets onto particle surfaces does not depend completely on whether droplets are introduced in the chamber based on simple settling or entrainment criteria. Several mechanisms contribute to deposition including inertial impaction, interception, Brownian diffusion, and electrostatic forces (Kraemer & Johnstone, 1955; Peters et al., 1982; Qian et al., 2004; Ushiki & Tien, 1984). Therefore, it is not sufficient to assess deposition efficiency (and thus process performance) using only rough entrainment calculations. Previous studies (Akbas et al., 2023, 2024; Mezhericher et al., 2020) demonstrating successful fluidized particle coating using aerosol droplets further support this observation.

The experiments were designed to maintain equivalent spray rates across the different atomization methods to ensure a consistent basis for comparison. Since the reference experiments was particle coating with aerosol (AG), to be able to compare the results from the experiments with the new nozzle and the Schlick nozzle, the volume flow rate of solution was set to 1.3 mL/min (NN1 and CN1), which was also the volume flow rate of solution from the aerosol generator with given atomizing air pressure and coating solution. The used aerosol coating experimental data (Akbas et al., 2024) had 2 h process time and 20 min sampling intervals. Therefore, to compare the results precisely, the aerosol-coated samples after 40 min were used, since at that time the consumed solution was 52 mL, which is the closest value to 60 mL (which is the total solution amount used for the experiments with the Schlick and the new nozzle, explained in Section 2.1.1).

Additionally, to observe its effect on particle coating, the volume flow rate of the coating solution was increased to 8.5 mL/min (NN2 and CN2). The atomizing air pressure was also increased accordingly from 1.5 bar to 4 bar to prevent cloggage in the nozzles and also produce precise spray inside of the fluidization chamber. Moreover, to observe coating by the new nozzle on different cores, additional experiments with $\gamma$-$Al_2O_3$ cores were conducted with 1.3 mL/min and 8.5 mL/min of coating solution volume flow rate (NN3 and NN4).

It should be noted that during experiments NN2 and NN4, cluster formation occurred on the nozzle tip due to sticking of localized overwetted fluidized particles. No such cluster formation was observed in experiment CN2 under the same atomizing conditions. The higher atomization pressure (1.5 → 4 bar) is the primary driver of the reduced droplet size in NN2 and NN4 relative to NN1 and NN3, consistent with the expected increase in relative gas-liquid velocity and associated Weber number. The increase in liquid flow rate (1.3 → 8.5 mL/min) primarily increases the liquid load in the nozzle region rather than substantially altering the droplet size. The simultaneous occurrence of both effects (finer droplets from elevated pressure and higher liquid loading from elevated flow rate) distinguishes NN2/NN4 from CN2, where the larger droplet size (longer evaporation time) at the same pressure and flow rate (Table 1) prevented rapid solid bridge formation. Furthermore, the Schlick nozzle's 0.8 mm orifice is inherently less susceptible to partial obstruction by adhered solid particles than the smaller orifice geometry of the new nozzle. At the lower flow rate (NN1 and NN3), no cluster formation occurred, demonstrating proper nozzle function. The experiments were not repeated to prevent potential damage to the new nozzle. No agglomeration or twinning was expected for the coating experiments, as the small droplet sizes employed which minimized the likelihood of particle-particle adhesion during the coating process, and no additional binder (such as HPMC) was used to increase the stickiness of the droplets on the particle surfaces.

**Table 2**
Spray rate and drying capacity ratio for the performed experiments.

| Experiment | Spray rate [g/min water] | Drying capacity ratio, $\dot{Q}_{dry}/\dot{Q}_{spray}$ [−] | Operating regime |
|---|---|---|---|
| NN1 | 0.91 | ~ 90 | Well below saturation |
| NN2 | 5.95 | ~ 9 | Below saturation |
| NN3 | 0.91 | ~ 72 | Well below saturation |
| NN4 | 5.95 | ~ 7 | Below saturation |
| CN1 | 0.91 | ~ 90 | Well below saturation |
| CN2 | 5.95 | ~ 9 | Below saturation |

### 2.3. Post-processing

#### 2.3.1. Calculation of coating coverage

A scanning electron microscope (SEM, Phenom G2 Pro) was used for taking pictures of 10 randomly selected particles out of samples at the end of each experiment. Same magnification value was used for all of the particle pictures. To detect coated parts on the surface of particles precisely, the contrast and the light were set individually. After taking the SEM pictures of particles, coverage percentages were calculated by considering the curvature effect, as in the studies of Akbas et al. (2023, 2024). This effect needs to be considered, since in reality the particles are spherical but the SEM pictures are planar. First, blurred parts near the edge of particles were removed, then 3D relative coverage of particles was calculated using a curvature index (Akbas et al., 2023). Corrections and calculations have been conducted using MATLAB image processing.

#### 2.3.2. Manual measurements of coating surface roughness and thickness using SEM pictures

As explained in Section 1, for the same amount of sprayed solid and process yield, the droplet size matters for the coating thickness distribution and surface roughness when full coverage has been reached. Therefore, after the calculation of coating coverage of experiments, the coating surface roughness and thickness measurements of coated particles were performed only for those with a coating coverage of more than 90% which are nearly fully coated (at the end of experiments NN1, NN2, NN3, CN1, and CN2, results in Section 3.2).

For each experiment, three SEM pictures of particles from the final sample were randomly selected for coating roughness evaluation. To calculate the surface roughness of a particle, its diameter was measured 36 times using ImageJ by rotating the measurement angle in 5° increments to 180° (180°/5° = 36 measurements per particle). To save time, the measured diameters were divided by two, assuming symmetry in the coating structure on both the upper and lower halves of the particle for intraparticle coated radius distribution.

The average coated surface roughness ($R_a$) of each particle was calculated as

$$R_a = \frac{\sum_{i=1}^{36} |\bar{r} - r_i|}{36}, \tag{1}$$

where $\bar{r}$ is the measured average radius of the coated particle and $r_i$ is the coated particle radius for the respective rotation angle. The average surface roughness of each experiment was then calculated by averaging the calculated surface roughness values ($R_a$) of the three coated

particles. The results will be discussed later in Section 3.3.

To measure the coating thickness of the particles, 20 random particles were selected from the sample at the end of the experiments only from those with a coating coverage of at least 90% (as like for the surface roughness investigation). After taking SEM pictures of these 20 particles individually, they were soaked into water (in 20 different cups, one for each particle) for 24 h to remove the coating material (NaB) from the surfaces. Then, they were dried into a laboratory oven for 24 h to get just the core particles. The SEM pictures of the core particles were taken.

To calculate the average coating thickness of particles, four diameter measurements by ImageJ (for 0°, 45°, 90° and 135°) were used instead of 36, as measuring the diameter 36 times for each particle was highly time consuming. To validate the reduced sampling for the calculation of coating thickness, results for the same particle were compared between the two sampling approaches (sampling of 4 and 36 diameters per particle). Measurement errors were calculated for the sampling of 4, taking the measurements by sampling of 36 as the real (correct) measurement. The errors of 0.45%, 0.57% and 4.79% were obtained for coated particle diameter, core particle diameter and coating thickness, respectively. As all error values are below 5%, the smaller sampling size (4 measurements) was sufficiently representative for calculating the average thickness of the products across the experiments (for 20 particles per experiment).

Fig. 4 shows SEM pictures of one of the coated particle at the end of experiment CN2 and the core of the same particle.

The coating thickness of the particle was calculated as half the difference of coated and core particle average diameters. To evaluate the average coating thickness for each experimental conditions, the measured average coating thickness of these 20 particles at the end of each experiment were used. All the results will be discussed in Section 3.4.1.

#### 2.3.3. Cutting the $\gamma$-$Al_2O_3$ particles for thickness investigation

For comparison with the manual coating thickness measurements explained in Section 2.3.2, individual particles with at least 90% coverage were selected and cut in half at their midpoint manually using a sharp knife to determine the coating thickness. This method was only applied successfully for $\gamma$-$Al_2O_3$ particles, since it was not possible to cut coated glass particles. SEM pictures of the equatorial planes of cut $\gamma$-$Al_2O_3$ particles were taken, and ImageJ was used for the direct measurement of the coating thickness from these SEM pictures.

#### 2.3.4. Measurements of coating thickness using laser diffraction

For the validation of the manual coating thickness measurement of coated glass particles (explained in Section 2.3.2), measurements by laser diffraction were performed, since glass particles could not be cut. A laser scattering particle size distribution analyzer (HORIBA Ltd., LA-960, Japan) was used to this purpose. For each experiment (NN1, NN2, CN1, CN2), an adequate quantity of particles from the final sample (at the end of the experiments) was provided to the analyzer. Measurements were conducted three times for each experiment, and the average of these three measurements was used to compare the particle sizes generated by different atomization methods.

To calculate the coating layer thickness, the size distribution of the glass cores (prior to the experiments) was also measured. The mean coating layer thickness for each experiment was calculated as half the difference between the mean size of the coated particles at the end of respective experiment and the mean size of the uncoated glass core particles.

Before using the device, refractive indexes of particles' surfaces were set. The refractive indexes were 1.51 and 1.45 for the measurement of glass (soda lime) cores and NaB-coated particles, respectively.

According to ISO 13320, the tolerances of the measurement for $d_{10}$, $d_{50}$ and $d_{90}$ are 3%, 2.5% and 4%, respectively. The device meets and exceeds these specifications, as confirmed by the manufacturer.

#### 2.3.5. Measuring process yield

To inquire the effect of different atomization methods on the particle coating, process yield was calculated for the experiments with glass cores. The measuring method was the same as in the studies of Akbas et al. (2023, 2024). At the end of the experiments, the product was split into five sample cups. Each cup was placed in a laboratory oven to dry, after which the dry mass of the coated particles was measured. Following this, the particles were soaked in distilled water for 24 h to remove the coating from the surface. Post-washing, they were dried again in the oven for 24 h to prepare for measuring the mass of the core particles. The yield for each sample was calculated, after upscaling to the total holdup, by dividing the actual coating mass deposited on the particles by the initial coating mass introduced into the fluidization chamber. The process yield for each experiment was then obtained by averaging the five individual yield values.

In the study by Akbas et al. (2024), measuring process yield was challenging for experiments using fresh $\gamma$-$Al_2O_3$ particles as cores. After washing the coated product with distilled water to remove the coating, the measured mass of the core particles was higher than their initial mass, leading to negative yield values, which are physically impossible. It was shown by Lefèvre et al. (2002) that there are three products of $\gamma$-$Al_2O_3$ hydration reaction: bayerite ($\beta$-$Al(OH)_3$), gibbsite ($\alpha$-$Al(OH)_3$) and boehmite ($\gamma$-AlOOH) that affect the surface stability and reactivity of $\gamma$-$Al_2O_3$ particles. In the study of Akbas et al. (2024), the fresh $\gamma$-$Al_2O_3$

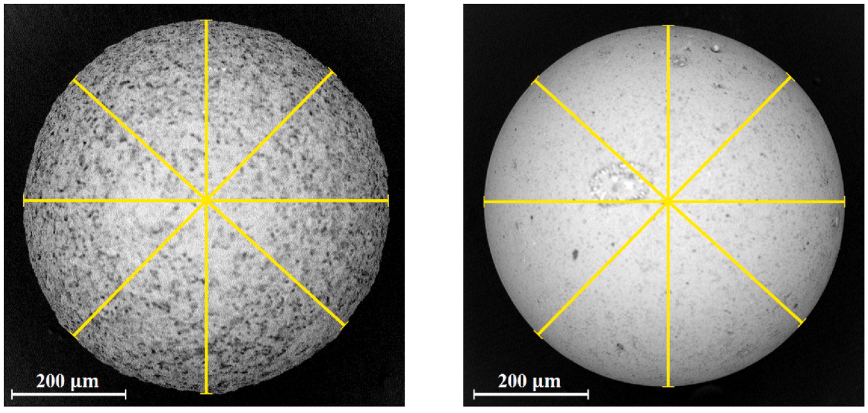


**Fig. 4.** SEM picture of (a) one of the coated glass particles at the end of experiment CN2, (b) the core of the same coated glass particle after washing. Scale bars: 200 µm.

particles were washed with distilled water and used as cores (after drying) for coating experiments to observe how the hydration affects aerosol droplet deposition. These experiments showed that hydration of fresh $\gamma$-$Al_2O_3$ particles before coating has a definite effect on aerosol droplet deposition and coating coverage, as well as on zeta potential of particles. Therefore, process yields were measured only for the experiments performed with glass cores (NN1, NN2, CN1, CN2), since the $\gamma$-$Al_2O_3$ cores were fresh (unwashed) in this study.

In Section 3.1, all the measured process yield values are presented.

## 3. Results and discussion

### 3.1. Process yield

The process yields were calculated (as explained in Section 2.3.5) for each coating experiment with the new nozzle and the Schlick nozzle. As expected, no agglomeration or twinning was observed in any of the experiments. For comparison, the process yield of the experiment with the aerosol generator (AG in Table 1) was taken from the study of Akbas et al. (2024). All the calculated process yields are shown in Fig. 5.

The yields of the experiments with the new nozzle (NN1 and NN2) are higher than the process yield of the aerosol coating experiment (AG). The main reason of coating material loss in aerosol coating experiments is that droplets dry early, before their deposition onto the particle surface, due to their smallness (0.9 μm mean diameter, see Table 1). This fact caused the aerosol droplets to be carried away as dust, so called overspray (Akbas et al., 2024). Therefore, less overspray with the new nozzle (since the droplet size provided by the new nozzle is bigger than the droplet size from the aerosol generator, Table 1) may be one of the reasons behind the higher process yield. Another reason might be the inlet position of the coating solution to the fluidization chamber. The aerosol droplets were introduced to the fluidized particles from the side of the fluidized bed ((Akbas et al., 2024), see also Fig. 3). However, with the new nozzle, they were supplied from the middle top of the fluidization chamber (see Fig. 1). This change might have influenced deposition efficiency as well as process yield. In total however, the new nozzle offers a clear advantage over aerosol generators by delivering higher process yield.

The yield of the new nozzle coating experiment with 1.3 mL/min solution flow rate (NN1) is similar to that of the conventional Schlick nozzle coating experiment with the same solution flow rate (CN1). The process yield was expected to increase with increasing volume flow rate of solution (as it happens from CN1 with process yield of 68.5% to CN2 with process yield of 91.2%) since atomizing air pressure was also increased accordingly (see Table 1). Previous studies of Mezhericher et al. (2017, 2019, 2020) show that the flow rate of droplets increases and the mean size of droplets decreases when the atomization air pressure rises (as also shown in the current study, Fig. 2). With increased flow rate, higher momentum of the droplets (i.e. more inertia) may lead to more deposition of droplets on the particle surface even if the droplet size decreases (which would mean higher process yield). In contrast, however, droplets of smaller size follow better the airflow due to reduced inertia, which could lead to lower droplet deposition and yield. Moreover, as droplet size decreases, it becomes more challenging to overcome surface potentials that would otherwise prevent deposition onto the particles (Akbas et al., 2024). The cluster formation on the nozzle tip during experiment NN2 (see Section 2.2) can also have affected the yield negatively. Therefore, when the flow rate increases to 8.5 mL/min with the new nozzle (NN2), the yield decreases to 35.9%.

It should be noted that, in our current process, recycling is not implemented. However, the overspray dust (consisting entirely of coating material) can in principle be collected, recycled, and reintroduced into the fluidized chamber to coat the particles. This recycling would significantly increase the overall process yield. Consistent with literature (Chiang & Tien, 1982; Paretsky et al., 1971; Pendse & Tien, 1982; Tien, 1982) showing that packed beds and fluidized beds can act as efficient dust collectors, the process yield can also be improved by increasing the particle inventory (Akbas et al., 2024).

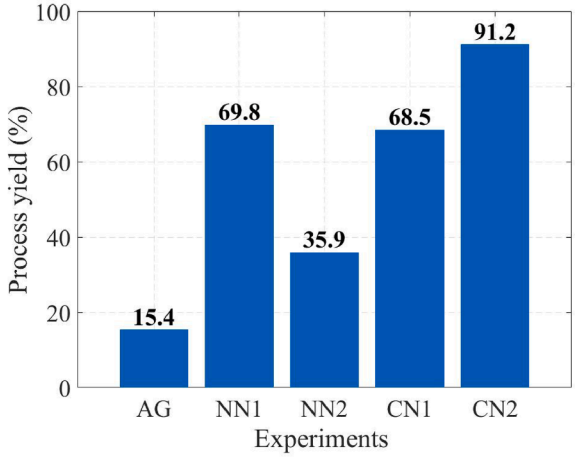


**Fig. 5.** Yields of experiments.

### 3.2. Coating coverages produced by different atomization methods

After the calculation of coating coverages of 10 particles for each experiments (as explained in Section 2.3.1), average and standard deviations of coating coverages were calculated. The average coverage values of products at the end of each experiment and their standard deviations are shown in Fig. 6. For the aerosol coating experiment (AG), the average coverage value at the end of 40 min process time was taken from the study of Akbas et al. (2024) (as explained in Section 2.2).

It can be observed from Fig. 6 that the coverage percentage at the end of the experiment with the new nozzle (NN1) was higher than the coverage with the aerosol generator (AG). This result was expected since the process yield of experiments with the new nozzle (NN1 and NN2) was higher than the process yield of the aerosol coating experiment (AG, see Fig. 5). Additionally, the footprint area of deposited droplets is bigger with the new nozzle, since those are bigger than aerosol droplets, which may lead to more coverage on the particle surface. It is, though, important to note that there is a 6-min difference in processing time between the aerosol-coated particles and those coated using the new nozzle (see Table 1). If samples had been taken after 46 min of aerosol coating, the coverage results would have been much closer (experiments AG and NN1). The coating coverage in the experiment with the new nozzle (NN1, 98.3%) was slightly higher than the coverage with the conventional Schlick nozzle (CN1, 95.0%), that has similar process

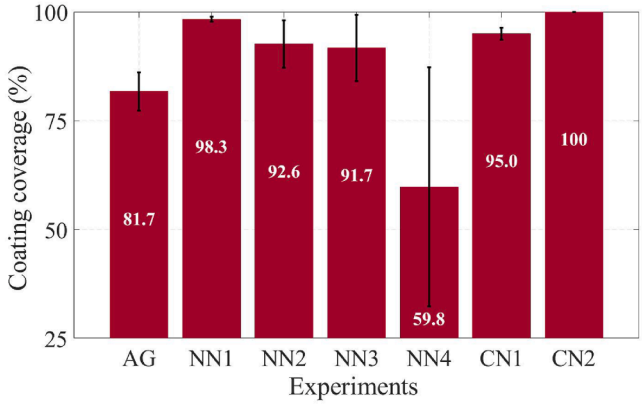


**Fig. 6.** The average coating coverage percentages on particle surfaces with standard deviations at the end of the experiments.

yield.

Similar to the study of Akbas et al. (2024), the coverage on fresh $\gamma$-$Al_2O_3$ particles (NN3 and NN4) was less than the coverage on glass particles (NN1 and NN2) for the same sypraying conditions because of the different zeta potential of core particles (−23.2 mV for glass particles, 17.3 mV for fresh $\gamma$-$Al_2O_3$ particles (Akbas et al., 2024)). With fresh $\gamma$-$Al_2O_3$ cores, the coverage seems to be larger than in (Akbas et al., 2024) by aerosol droplets. The main reason is the different atomization methods. The new nozzle in this study produces bigger droplets than the aerosol generator. Smaller droplets from the latter (as in (Akbas et al., 2024)), can more easily be affected from the surface charge of the core particles negatively, that may impede deposition on the core particle surface. When the droplet size gets bigger (as in this study with the new nozzle), inertia becomes dominant. That may cause droplets to overcome the electrostatic forces and, therefore, more easy deposit on particle surface (which means more coverage). However, the zeta potential of core particles has still an effect on the droplet deposition even the droplet size is bigger in this study, since the coverage on fresh $\gamma$-$Al_2O_3$ particles (NN3 and NN4) is less than the coverage on glass particles (NN1 and NN2), with approximately same number of particles (common total surface area to be coated) inside of the fluidization chamber for all experimental settings (experiments with glass particles: 1000 g bed mass with 2500 kg/m$^3$ particle density, with $\gamma$-$Al_2O_3$ particles: 600 g bed mass with 1280 kg/m$^3$ particle density).

Surface roughness of core particle is another parameter that may influence droplet deposition, and consequently, coating coverage. Numerous studies in the literature have examined the relationship between core surface roughness and droplet behavior upon deposition. For instance, Quetzeri-Santiago et al. (2019) explored the impact of surface roughness on the splashing dynamics of droplets, while Wenzel (1936) investigated the resistance of rough surfaces to wetting. Similarly, Cassie and Baxter (1944) analyzed the effect of surface roughness on contact angles, showing that rough surfaces tend to increase the contact angle between the solid surface and the deposited droplet. As a result, rough surfaces lead to a smaller droplet footprint area compared to smoother ones. In the present study, the average surface roughness ($R_a$) of glass particles ranged from 35 nm to 45 nm, as provided by the manufacturer. Based on literature findings, the surface roughness of $\gamma$-$Al_2O_3$ particles is likely within the high nanometer to low micrometer scale (Jahanshahi et al., 2023; Sharma et al., 2019), indicating that the porous $\gamma$-$Al_2O_3$ surface is rougher than that of the glass particles. Previous studies conducted in our department, which measured the contact angles of pure water and aqueous HPMC solutions on both glass and $\gamma$-$Al_2O_3$ particles, demonstrated that the contact angle is not significantly influenced by the concentration of dissolved solids, even when compared with pure water (Terrazas-Velarde, 2010). Instead, the results showed that the contact angle is primarily determined by the surface characteristics of the substrate. Smooth surfaces exhibit smaller contact angles, whereas rough surfaces exhibit larger ones. The measured contact angles were approximately 40° for glass particles and 60° for $\gamma$-$Al_2O_3$ particles (Terrazas-Velarde et al., 2009, 2011a), in good agreement with values reported in the literature (Chunsheng et al., 2008; Mao et al., 1997; Redón et al., 2005). Since no correlation was observed between contact angle and solute concentration, and the NaB solution used in this study is water-based, the expected contact angles for droplets in our experiments are approximately 40° on glass and 60° on $\gamma$-$Al_2O_3$ particles. Consequently, due to the reduced footprint area of droplets (bigger contact angle) on the rougher $\gamma$-$Al_2O_3$ surface, a higher coating coverage may be expected on the smoother glass particles (apart from the affect of zeta potential of core materials on droplet deposition), given the same number of deposited droplets.

The zeta potential of the particles influences droplet deposition efficiency, particularly for small droplets. It affects the overall process yield, the particle coverage, and even the storage stability after coating (Akbas et al., 2024). When the droplets become larger, inertial forces dominate, and the effect of zeta potential on droplet deposition becomes negligible. While electrowetting (manipulating contact angles by applying voltage) has been studied for several liquids and surfaces (Mugele & Baret, 2005; Teng et al., 2020), to our knowledge no study has systematically investigated the influence of droplet or substrate electrostatic charge on the contact angle (or the footprint area) of NaB droplets on glass or $\gamma$-$Al_2O_3$ surfaces. Conceptually, if a droplet and deposited surface carry the same charge, the repulsive electrostatic forces during drying could lead to an increase in the final droplet height and a reduction in the footprint area. Conversely, if they carry opposite charges, attractive forces during drying may decrease the dried droplet height and increase the footprint area. However, a detailed and systematic investigation would be necessary to draw certain conclusions about the specific influence of zeta potential on the drying behavior of deposited droplets especially for small sizes used in this study. On the other hand, there was a cluster formation on the new nozzle when the solution flow rate was increased (Section 2.2) that affects the coating process as well as the coverage negatively.

For experiments with both glass and $\gamma$-$Al_2O_3$ particles, when the solution flow rate increased form 1.3 mL/min (NN1 and NN3) to 8.5 mL/min (NN2 and NN4) the standard deviation of the particle coverage got bigger (see Fig. 6), which means that the coating became interpartically uneven. The atomizing air pressure was increased from 1.5 to 4 bar when increasing the solution flow rate from 1.3 to 8.5 mL/min (see Table 1). Therefore, this increased atomizing pressure leads to a decrease in the angle of the nozzle spray, thus leading to a narrower spray zone for particles inside the fluidization chamber. As a result of this fact, at the end of experiments NN2 (for glass particles) and NN4 (for $\gamma$-$Al_2O_3$ particles) interparticle uniformity of coating was worse than in the experiment NN1 (for glass particles) and NN3 (for $\gamma$-$Al_2O_3$ particles), respectively, even if the particles were continuously mixed during the fluidization inside of the chamber. The cluster formation on the nozzle during experiment NN4 (see Section 2.2) may additionally have contributed to interparticle non-uniformity of coating. This effect is also visible in Fig. 6, where NN4 shows a high standard deviation. Additionally, the process time at increased solution flow rate was dramatically shorter (7 min) than the process time with slow flow rate of solution (46 min). Consequently, particles experienced fewer exposures to droplets in the narrower spray zone under higher solution flow rates during the 7-min process compared to the exposures in the wider spray zone at slower flow rates during the 46-min process, especially as particles travel from the fluidization chamber wall to the center of the fluidized bed while mixing. The combination of the narrower spray zone and the reduced process time with the increased flow rate resulted in more uneven coating coverage among particles.

It was not possible to see this effect for the coating experiments with the Schlick nozzle since all the particles were fully (100%) coated at the end of the experiment with increased flow rate of solution (CN2).

### 3.3. Structures of coating produced by different atomization methods

After measuring coated particle diameters 36 times, as explained in Section 2.3.2, radius values at the respective rotation angles were graphed alongside with corresponding radii of their cores. Exemplarily, Fig. 7 shows such results for one of the evaluated particles with a coating coverage more than 90% at the and of each of in total five experiments.

The surface roughness of the coated particles is determined by the building block (BB) height, which corresponds to the height of a dried droplet on the particle surface. After deposition, each droplet forms a wet spherical cap. The cap height is a function of the contact angle and initial droplet size. According to the literature (Terrazas-Velarde et al., 2011a, 2011b), for droplets of identical size, the BB height depends on several parameters. These parameters include the deposited wet height, temperature, fluidization velocity (through the mass transfer coefficient), contact angle, droplet solution, and fluidization gas properties (Terrazas-Velarde et al., 2011a). Larger droplets produce greater spherical cap heights for the same contact angle. Therefore, under

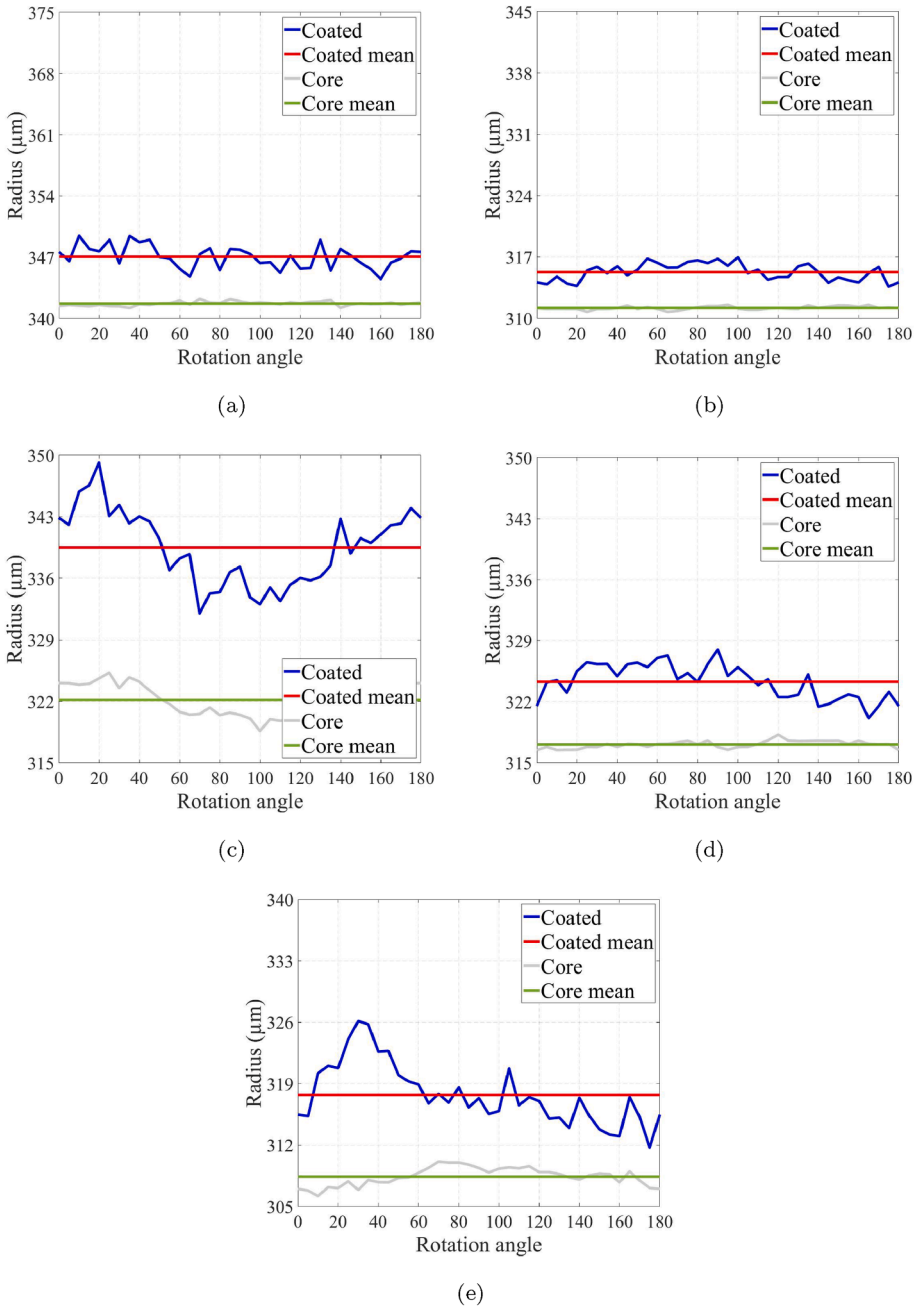


**Fig. 7.** Graph of surface structure of a glass particle at the end as well as at the beginning of experiment (a) NN1, (b) NN2 with the new nozzle; (c) CN1, (d) CN2 with the conventional Schlick nozzle; (e) a $\gamma$-$Al_2O_3$ particle from experiment NN3.

identical conditions, the resulting BB height is larger compared to that formed by smaller droplets. Even in the case of extremely rapid drying (very short drying time), the BB height remains limited by the spherical cap height. Therefore, smaller droplets will still produce smaller BB heights and thus smoother surfaces even if drying occurs very quickly. In the present study, regarding drying kinetics, the only parameters that could influence the dried height of droplets of equal size are the fluidization velocity and the contact angle, as the temperature (50 °C), coating solution (NaB), and fluidization gas properties were identical across all experiments. The fluidization gas flow rates ranged from 40 kg/h to 50 kg/h. However, this variation has a negligible effect on the BB height, since the fluidization velocity influences it only indirectly through the mass transfer coefficient. Therefore, the contact angle is the primary parameter governing the BB height for the droplets of same size in this study. With contact angles of 40° and 60°, far away from complete wetting, the spreading time is considered to be very small. Consequently, the coarsening effect by droplets that dry before they could spread is considered to be small. Due to the larger contact angle on the $\gamma$-$Al_2O_3$ surface (60°) compared to that on the glass surface (40°), a rougher coating surface was expected on the $\gamma$-$Al_2O_3$ particles for the same droplet size, resulting from the formation of higher BB structures.

The surface structure of a single dried droplet (a single BB) indeed influences the final coating roughness. When NaB solution is used as the coating liquid, the surface of an individual BB is expected to be rough due to crystallization during drying, compared to a polymeric coating. However, given the very small droplet sizes employed in our coating process, the dominant factor determining the overall coating roughness is the BB height rather than its fine scale surface texture. For the same droplet size and particle surface (the same contact angle (Section 3.2), and consequently the resulting BB height), would be similar for both

polymeric and NaB solutions. Therefore, when larger droplets are used, the BB height increases, leading to a rougher coating surface, even if a polymeric solution is used instead of NaB.

The reason polymer coatings appear smooth is that the process temperature is brought above the so-called film formation temperature (either intentionally increased during coating or in a subsequent post-processing step), which corresponds to the glass transition temperature of the polymer. At this temperature, the coating material softens and can flow, producing compact and uniform coatings even from coatings that initially have been rough and non-uniform (Sondej et al., 2015).

The average coating roughness of each experiment was calculated for three particles as explained in Section 2.3.2, and its variation across experiments is shown in Fig. 8. The vertical lines represent the ranges of measured coating roughness, while the dot markers indicate the mean values.

Experiment CN1 with the Schlick nozzle exhibits the highest coating roughness range (1.40 μm to 3.65 μm), suggesting a relatively rough and uneven coating. When the atomizing pressure increased in experiment CN2 (with a Sauter mean droplet diameter of around 12 μm), the range became narrower compared to CN1 (with a Sauter mean droplet diameter of around 22 μm), due to smaller droplets.

Experiment NN2 with the new nozzle and increased atomizing pressure (Sauter mean droplet diameter of 7.07 μm) has the lowest range of coating roughness values (0.82 μm to 1.88 μm), indicating a smoother coating structures compared to other experimental conditions. At smaller atomizing pressure, NN1 (Sauter mean droplet diameter of 12.5 μm), the coating became rougher, due to bigger droplets than in NN2. When the core material changed from glass (NN1) to $\gamma$-$Al_2O_3$ (NN3) under same spraying conditions, the range got wider indicating rougher coating on $\gamma$-$Al_2O_3$ cores. As explained in Section 3.2, rough surface of $\gamma$-$Al_2O_3$ cores (compared to glass cores) leads to reduced footprint area of deposited droplets, therefore increased height of building blocks. This fact causes the coating surface roughness increase on $\gamma$-$Al_2O_3$ cores, as observed in the current study.

For the same experimental conditions, the mean coating roughness provided by the new nozzle (NN1 and NN2) was smaller than the one provided by the Schlick nozzle (CN1 and CN2), aligning with their wider roughness ranges. With the lower mean and narrower range of roughness values, the new nozzle can produce intrapartically and interpartically more homogeneous coated products compared to the conventional Schlick nozzle. The findings align with our expectations.

While detailed aerodynamic analysis using dimensionless groups (e.g., Weber number, air/liquid ratios) typically requires explicit nozzle geometric parameters which are proprietary in this case, the measured droplet size distributions reported here serve as the primary quantitative basis for the analysis. The results demonstrate a direct correlation between the reduced droplet size achieved by the new nozzle and the resulting surface roughness and coating thickness (Section 3.4), independent of the internal nozzle design mechanics.

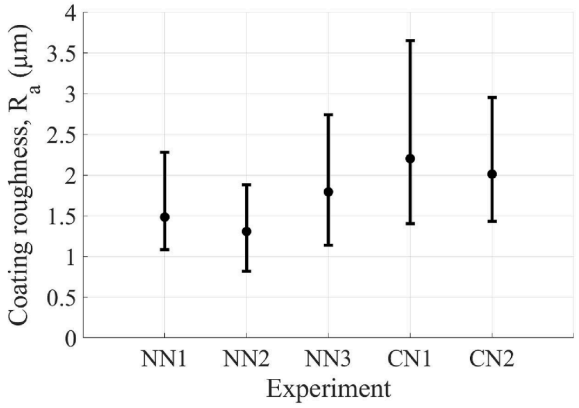


**Fig. 8.** Variation of coating roughness across experiments.

### 3.4. Interparticle coating thickness distributions

#### 3.4.1. Manual measurements

Following the manual measurement of the coating thickness (20 particles for each experiment, 4 diameters measured for each particle, as detailed in Section 2.3.2), cumulative normal coating thickness distribution functions based on the number of particles were plotted (by using the mean and standard deviations of the 20 particles' average coating thickness) for the experiments NN1, NN2, NN3 (using the new nozzle), and CN1, CN2 (using the Schlick nozzle) as shown in Fig. 9.

The mean coating thickness on glass particles from the experiments with small volume flow rate of solution (1.3 mL/min) was 6.85 μm for the new nozzle (NN1, Sauter mean droplet diameter of 12.5 μm) and 19.0 μm for the conventional Schlick nozzle (CN1, Sauter mean droplet diameter of around 22 μm). When the flow rate increased to 8.5 mL/min, the mean coating thickness decreased to 2.96 μm for the new nozzle (NN2, Sauter mean droplet diameter of 7.07 μm) and to 6.54 μm for the conventional Schlick nozzle (CN2, Sauter mean droplet diameter of around 12 μm). With the smaller droplets by increased atomizing air pressure, resulting in thinner coating layers on the nearly fully coated particles in the higher flow rate experiments (NN2 and CN2). The coating thickness of $\gamma$-$Al_2O_3$ particles (NN3) was similar to that of glass particles (NN1) under the same experimental conditions.

Under identical fluidized bed operating conditions, the new nozzle produced significantly smaller droplets (~10 μm) compared to the conventional Schlick 970/0 S4 nozzle (~20 μm) as shown in Table 1 and Fig. 2. This performance demonstrates that the new nozzle bridges the capability gap between ultrafine aerosol generators (~1 μm, low throughput) and standard commercial two-fluid nozzles (20 to 40 μm), allowing for thinner and smoother coatings while maintaining process feasibility.

The coating thickness by aerosol ranges from 1 to 6 μm for particles that are fully (100%) coated (Akbas et al., 2024; Mezhericher et al., 2020). In the current study, the coating layer thicknesses generated by the new nozzle (NN1 and NN2) are comparable to those of aerosol coated particles. However, it is important to note that the particles coated with the new nozzle, in this study, are not exactly 100% coated (see Fig. 6, more than 90% coated). If it was possible to perform the experiments for the new nozzle with a larger amount of solution or a longer process time, the particles would have exhibited thicker coatings with 100% surface coverage.

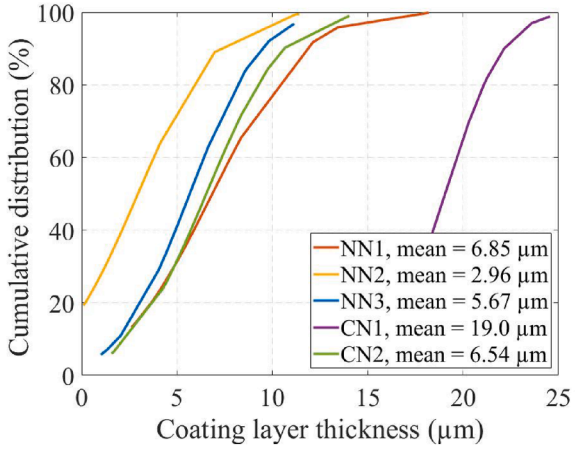


**Fig. 9.** Number-based cumulative coating thickness distribution of glass particles at the end of experiments.

### 3.4.2. Measurements by using laser diffraction

In addition to the manual coating thickness measurements, the coating layer thickness for each experiment with glass cores was determined using laser scattering. The cumulative particle size distributions measured by laser diffraction (as detailed in Section 2.3.4) and calculated layer thicknesses are presented in Fig. 10.

The coating layer thickness on the glass particles from the experiment using the new nozzle with 8.5 mL/min solution flow rate (NN2, Sauter mean droplet diameter of 7.07 μm) was measured as 8.88 μm, which is the thinnest layer measured. Similar coating layer thicknesses were measured for the experiment using the new nozzle with 1.3 mL/min solution flow rate with a Sauter mean droplet diameter of 12.5 μm (NN1, 11.5 μm mean layer thickness) and the experiment using conventional Schlick nozzle with 8.5 mL/min solution flow rate with a Sauter mean droplet diameter of around 12 μm (CN2, 10.7 μm mean layer thickness). The thickest coating layer on the glass particles was obtained from the experiment using the Schlick nozzle with 1.3 mL/min solution flow rate with Sauter mean droplet diameter of around 22 μm (CN1, 13.3 μm mean layer thickness).

The layer thickness trends acquired from laser scattering match the manual thickness measurements with some numeric differences. As explained in Section 2.3.4, the used laser scattering particle size distribution analyzer has tolerances. In Fig. 10, the blue and red shadows around the cumulative curves represent the error zones (according to the tolerance values of the analyzer, see Section 2.3.4) of the size measurement of glass cores and coated glass particles, respectively. For example, the mean size of glass cores was measured as 615 μm with laser scattering. This differs from the value measured by CAMSIZER mentioned in Section 2.1.2, since the used HORIBA laser scattering device measures particle size distributions first based on volume of particles and then converts the measurement into number based particle size distribution. Therefore, there may be some differences between size measures from CAMSIZER and HORIBA. With the 2.5% tolerance for $d_{50}$ (Section 2.3.4), the size measurements of HORIBA might range in 615 ± 15 μm. In that case, the used laser scattering device may not determine the size enlargement caused by coating layers that has a 7.5 μm thickness and below, since these coating thickness values are in the tolerance range of the device. As it may be observed from Fig. 10, the tolerance ranges of core glass particles and coated particles are overlapping. This situation makes the manual measurements more reliable for such thin coating layers.

Other than the tolerance range of the device, the fact that the particles are not fully covered may likely cause an additional error in particle size measurements with the principle of laser scattering. In the use of laser scattering, when the particles are not 100% covered yet (which means different properties partially on the particle surface), additional measurement error may occur because of the different refractive indexes (see Section 2.3.4) of the core particle surface (glass) and coating material (NaB). Moreover, the particle surface roughness (Fig. 8) may create an additional effect of multiple light reflections that interfere with laser beam scattering and result in measurement error. Therefore, the particle size measurement error of laser scattering with those not 100% coated particles is likely above 2.5% (provided by the manufacturer), and the roughness of particles introduces additional uncertainty.

### 3.4.3. Coating thickness evaluation for $\gamma$-$Al_2O_3$

The coated $\gamma$-$Al_2O_3$ particles were cut through their center, as explained in Section 2.3.3, to obtain the thickness of coating layer. Exemplary pictures are shown in Figs. 11 and 12 from the experiments using $\gamma$-$Al_2O_3$ cores with 1.3 mL/min (NN3) and 8.5 mL/min (NN4) solution flow rate, respectively.

By cutting the particles, it is possible to retrieve intraparticle coating layer thickness distributions. However, it needs to be noted that the here given layer thickness values are only indicative and intraparticle layer thickness distributions have not been investigated in the present work.

As seen in Fig. 11, the coating layer is not uniform. Although the particles are not fully coated yet (Fig. 6), the preferential deposition on already occupied areas of the particle surface, as investigated by Akbas et al. (2023), plays a role in creating a wavy structure of the coating layer. The indicative measured coating thickness values are 3.5 and 1.6 μm. The manual thickness measurements of NN3 (with a Sauter mean droplet diameter of 12.5 μm) ranged from 1 μm to 11 μm, with an average thickness of 5.67 μm (Fig. 9). The indicative coating thickness obtained from cut particles was, thus, consistent with the manually measured thickness values.

Although the average coverage at the end of the experiment NN4 was only 59.8%, one of the most covered $\gamma$-$Al_2O_3$ particles (that had around 90% coverage, the coverage range can be observed from Fig. 6) was selected from the sample at the end of the experiment NN4 to be cut for the coating thickness evaluation. The respective SEM picture of the particle is represented in Fig. 12.

As the solution flow rate increased in NN4 (with a Sauter mean droplet diameter of 7.07 μm), the indicative coating thickness decreased to 1.4 μm (Fig. 12) that is closer to the aerosol coating thickness with full coverage in the study of Akbas et al. (2024). This reduction in coating thickness is attributed to the smaller droplet size generated by the increased solution flow rate and atomization pressure, resulting in smaller building blocks on the surface and, consequently, thinner coating layers. Although the measured thicknesses are relatively small with the new nozzle, it is important to note that the particles were not fully covered yet. If the process time had been extended, the resulting layer thickness would have been thicker with full surface coverage.

## 4. Conclusion

The main purpose of this study was to investigate coated particles by

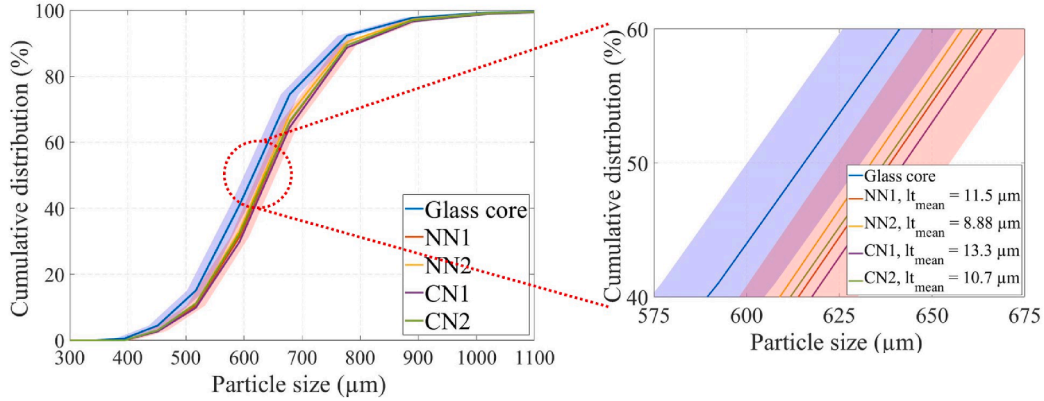


**Fig. 10.** Number based cumulative particle size distribution of core and coated particles at the end of experiments with glass cores (lt: layer thickness).

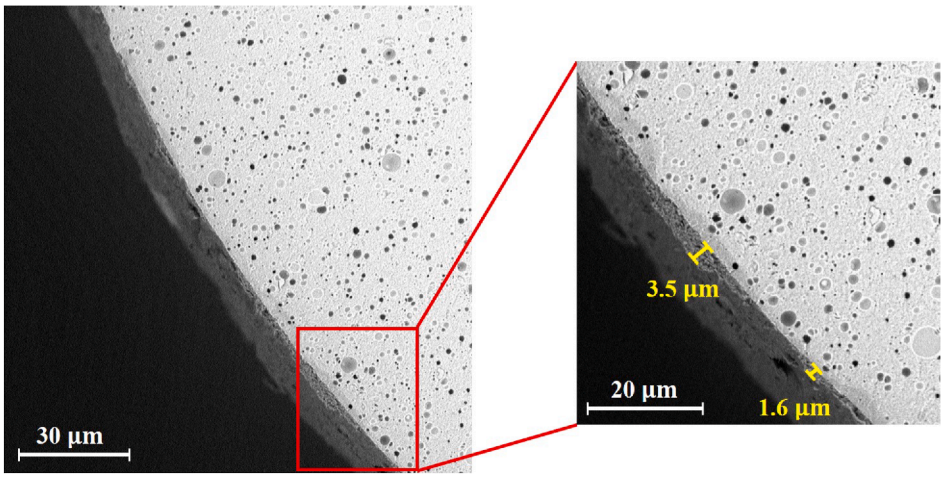


**Fig. 11.** SEM picture of a cut $\gamma$-$Al_2O_3$ particle at the end of the experiment NN3. Scale bars: 30 µm and 20 µm.

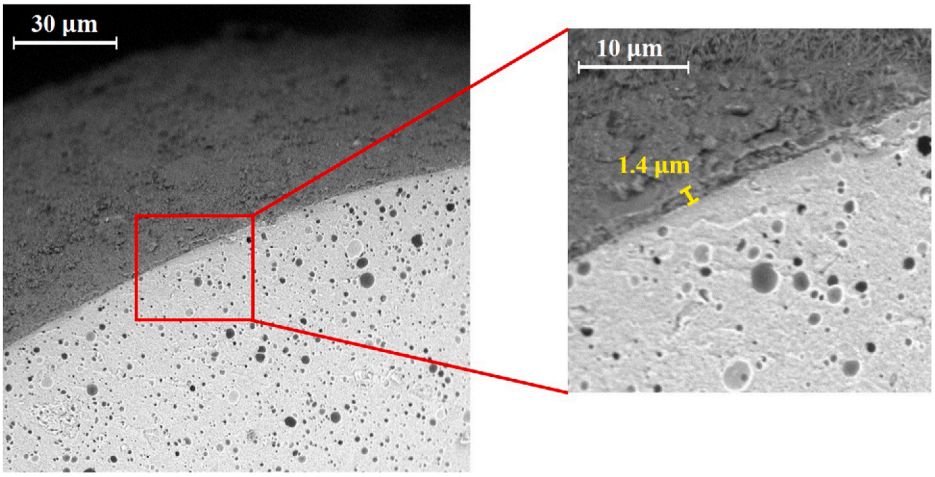


**Fig. 12.** SEM picture of a cut $\gamma$-$Al_2O_3$ particle at the end of the experiment NN4. Scale bars: 30 µm and 10 µm.

a new three-channel coaxial nozzle, that can produce droplets smaller than the conventional Schlick nozzle, in terms of the coating coverage, thickness and surface roughness, as well as yield of coating processes. Several coating experiments in fluidized bed with these atomization methods were performed with two different solution flow rates (1.3 and 8.5 mL/min) and atomization pressures (1.5 and 4 bar). The results of process yield, coating coverage, thickness and coating structures of particles coated by these different atomization methods were compared. The coating coverage and process yield results were additionally compared with aerosol coating experiments performed in (Akbas et al., 2024).

When the yields of the coating processes with different atomization methods that have the same solution flow rate and atomizing pressure are compared, the process yield of the experiment with the new nozzle (NN1, 69.8%) is similar to the one with the conventional Schlick nozzle (CN1, 68.5%) and is higher than the one with the aerosol generator (AG, 15.4%). It was expected to have higher process yield when the solution flow rate increases (as with the use of the conventional Schlick nozzle, CN2, 91.2%) because of the increased momentum of droplets. This was not the case with the new nozzle and the process yield decreased to 35.9% due to the cluster onto the nozzle tip that is a result of localized over-wetted fluidized particles as well as the reduced inertia caused by reduced droplet size from 12.5 µm to 7.07 µm. It was not possible to measure the process yield for the experiments with $\gamma$-$Al_2O_3$ cores (NN3 and NN4) since they were fresh (unwashed before the experiments).

For the same solution flow rate, even if the process yield of the coating experiment with the new nozzle (NN1, 69.8%) was dramatically higher than the one with aerosol generator (AG, 15.4%), the difference in term of coating coverage was not that big (81.7% and 98.3% for aerosol generator and the new nozzle, respectively), also with 6 min sampling shortage of the aerosol coating process. With similar process yields of the coating processes with the new nozzle (NN1) and the Schlick nozzle (CN1), the coating coverage obtained from the new nozzle (98.3%) was slightly higher than the coverage with the Schlick nozzle (95.0%). The coating coverage was lower on the fresh $\gamma$-$Al_2O_3$ particles than on the glass particles in experiments with same conditions using approximately same number of particles to coat. The main reasons were the difference in zeta potential and roughness of core particle surfaces.

In terms of the surface structure of coated particles, under the same experimental conditions, the mean coating roughness produced by the new nozzle (NN1 and NN2) was lower than that of the Schlick nozzle (CN1 and CN2), consistent with their broader roughness ranges. Due to its lower mean and narrower roughness distribution, the new nozzle can produce coatings with higher homogeneity compared to the conventional Schlick nozzle.

Manual thickness measurement results show that, with the new nozzle, it is possible to coat particles thinner (NN1, mean thickness of 6.85 µm) than with the conventional Schlick nozzle (CN1, mean thickness of 19.0 µm) with more than 90% coverage in a quite short process

time of 46 min. Moreover, with the new nozzle, it was possible to decrease the mean coating thickness by increasing solution flow rate and atomizing pressure that leads to decrease in droplet size that the new nozzle creates. Although the particles were not fully covered (but more than 90% covered) for the thickness measurements, these results are representative and certainly give an idea about the coating thickness with full coverage. Thickness measurements using laser diffraction support the manual thickness measurements.

In conclusion, proof-of-principle experiments demonstrated that the new nozzle offers a promising alternative for achieving thinner and smoother coatings than conventional spray coating by generating droplets with a mean diameter of approximately 10 μm. This bridges the gap between aerosol (around 1 μm) and conventional nozzles (around 20 μm, even bigger). With its ability to produce smaller droplets than conventional nozzles, and provide higher process yield than aerosol fluidized bed particle coating, the new nozzle shows significant potential for fluidized particle coating applications particularly for industries requiring ultrathin coatings such as pharmaceuticals, chemicals, and biochemicals.

For future works, the present study can be improved in several directions. The experimental setup can be improved to prevent cluster formation especially for the new nozzle. Experiments should address full coverage conditions by simply increasing the process time to measure coating thickness more precisely in future investigations. The fresh $\gamma$-$Al_2O_3$ cores needs to be washed before performing experiments or different material cores that has different surface potential can be used to observe the zeta potential effect when the droplet size is bigger than aerosol droplets, as like with the new nozzle. Additionally, the influence of zeta potential on the drying behavior of deposited droplets can be systematically investigated to evaluate its effect on BB height and footprint area, particularly for small droplets. Experiments can be conducted at different process temperatures to investigate their effect on the BB height and, consequently, on the resulting coating surface structure. A different coating liquid, such as a polymer-based solution, can be used to investigate how variations in the drying mechanism (polymerization rather than crystallization) affect the overall coating surface roughness. Moreover, the experimental results of surface coverage and interparticle as well as intraparticle coating layer thickness distributions can be supported by Monte Carlo simulations. Furthermore, the measured process yield values can be acquired with a continuous model. From an application standpoint, future studies could also explore the application of the new nozzle technology in industries where ultrathin coatings are essential. Potential areas include pharmaceuticals for improved coating uniformity, energy storage for precise electrode material coating and functional coatings for catalyst supports in the chemical industry.

## CRediT authorship contribution statement

**Serap Akbas:** Writing – original draft, Visualization, Software, Investigation, Formal analysis, Data curation. **Maksim Mezhericher:** Writing – review & editing, Validation, Resources, Investigation, Data curation, Conceptualization. **Torsten Hoffmann:** Supervision, Investigation, Data curation. **Nikolay Razorenov:** Data curation. **Zehao Pan:** Data curation. **Evangelos Tsotsas:** Writing – review & editing, Validation, Supervision, Project administration, Funding acquisition, Conceptualization.

## Declaration of competing interest

The authors declare the following financial interests/personal relationships which may be considered as potential competing interests: Serap Akbas reports financial support was provided by Deutsche Forschungsgemeinschaft (DFG, German Research Foundation). The authors declare that they have no known competing financial interests or personal relationships that could have appeared to influence the work reported in this paper.

## Acknowledgements

The authors gratefully acknowledge the financial support of this work by Deutsche Forschungsgemeinschaft (DFG, German Research Foundation) - Project number: 452247553. We also would like to thank Dr. Junshi Wang (Princeton University) for his assistance in measuring and analyzing the droplet size distributions generated by the new nozzle.

## Abbreviations

| | |
|---|---|
| $\gamma$-$Al_2O_3$ | gamma alumina |
| $\beta$-$Al(OH)_3$ | bayerite |
| $\alpha$-$Al(OH)_3$ | gibbsite |
| $\gamma$-AlOOH | boehmite |
| AFB | aerosol fluidized bed |
| AG | aerosol generator |
| BB | building blocks |
| CN | conventional Schlick nozzle |
| lt | layer thickness |
| NaB | sodium benzoate |
| NN | new nozzle |
| PVC | polyvinyl chloride |
| $R_a$ | average surface roughness |
| SEM | scanning electron microscopy |
| SFB | spray fluidized bed |

## References

Akbas, S., Chen, K., Hoffmann, T., Scheffler, F., & Tsotsas, E. (2023). Investigation of island growth on fluidized particles coated by means of aerosol. *Processes, 11*, 165. https://doi.org/10.3390/pr11010165. URL: https://www.mdpi.com/2227-9717/11/1/165.

Akbas, S., Zhang, J., Hoffmann, T., & Tsotsas, E. (2024). Aerosol fluidized bed coating: Exploring the impact of process conditions on process yield, coating coverage and thickness. *Chemical Engineering Journal, 495*, Article 153349. https://doi.org/10.1016/j.cej.2024.153349. URL: https://www.sciencedirect.com/science/article/pii/S1385894724048381.

Bérengère Guignon, A. D., & Dumoulin, E. D. (2002). Fluid bed encapsulation of particles: Principles and practice. *Drying Technology, 20*, 419–447. https://doi.org/10.1081/DRT-120002550. URL:.

Capece, M., & Dave, R. (2011). Application of fluidized bed film coating for membrane encapsulation of catalysts. *Powder Technology, 211*, 199–206. https://doi.org/10.1016/j.powtec.2011.04.015. URL: https://www.sciencedirect.com/science/article/pii/S0032591011001987.

Cassie, A. B. D., & Baxter, S. (1944). Wettability of porous surfaces. *Transactions of the Faraday Society, 40*, 546–551. https://doi.org/10.1039/TF9444000546. URL:.

Chiang, H.-W., & Tien, C. (1982). Deposition of brownian particles in packed beds. *Chemical Engineering Science, 37*, 1159–1171. https://doi.org/10.1016/0009-2509(82)85060-4. URL: https://www.sciencedirect.com/science/article/pii/0009250982850604.

Chunsheng, R., Dezhen, W., & Younian, W. (2008). Grafting silane onto silicate glass surface treated by DBD in air. *Plasma Science and Technology, 10*, 556. https://doi.org/10.1088/1009-0630/10/5/07. URL:.

Culver, S. P., Koerver, R., Zeier, W. G., & Janek, J. (2019). On the functionality of coatings for cathode active materials in thiophosphate-based all-solid-state batteries. *Advanced Energy Materials, 9*, Article 1900626. https://doi.org/10.1002/aenm.201900626. URL: https://onlinelibrary.wiley.com/doi/abs/10.1002/aenm.201900626.

Dumouchel, C., Yongyingsakthavorn, P., & Cousin, J. (2009). Light multiple scattering correction of laser-diffraction spray drop-size distribution measurements. *International Journal of Multiphase Flow, 35*, 277–287. https://doi.org/10.1016/j.ijmultiphaseflow.2008.11.001. URL: https://www.sciencedirect.com/science/article/pii/S0301932208001663.

Jahanshahi, M., Mofidian, R., Hosseini, S., & Miansari, M. (2023). Investigation of mechanical properties of granular $\gamma$-alumina using experimental nano indentation and nano scratch tests. *SN Applied Sciences, 5*, 164. https://doi.org/10.1007/s42452-023-05388-7

Janocha, M., & Tsotsas, E. (2022). In-depth investigation of incremental layer build-up from dried deposited droplets. *AIChE Journal, 68*, Article e17445. https://doi.org/10.1002/aic.17445. URL: https://aiche.onlinelibrary.wiley.com/doi/abs/10.1002/aic.17445.

Kieckhefen, P., Lichtenegger, T., Pietsch, S., Pirker, S., & Heinrich, S. (2019). Simulation of spray coating in a spouted bed using recurrence cfd. *Particuology, 42*, 92–103. https://doi.org/10.1016/j.partic.2018.01.008. URL: https://www.sciencedirect.com/science/article/pii/S1674200118300956.

Kleinbach, E., & Riede, T. (1995). Coating of solids. *Chemical Engineering and Processing: Process Intensification, 34*, 329–337. https://doi.org/10.1016/0255-2701(94)04021-4. URL: https://www.sciencedirect.com/science/article/pii/0255270194040214.

Kraemer, H. F., & Johnstone, H. F. (1955). Collection of aerosol particles in presence of electrostatic fields. *Industrial & Engineering Chemistry, 47*, 2426–2434. https://doi.org/10.1021/ie50552a020. URL:.

Lefèvre, G., Duc, M., Lepeut, P., Caplain, R., & Fédoroff, M. (2002). Hydration of $\gamma$-alumina in water and its effects on surface reactivity. *Langmuir, 18*, 7530–7537. https://doi.org/10.1021/la025651i. URL: https://api.semanticscholar.org/CorpusID:35459896.

Liu, Y.-H., Calvert, G., Hare, C., Ghadiri, M., & Matsusaka, S. (2012). Size measurement of dry ice particles produced from liquid carbon dioxide. *Journal of Aerosol Science, 48*, 1–9. https://doi.org/10.1016/j.jaerosci.2012.01.007

Mao, T., Kuhn, D. C. S., & Tran, H. (1997). Spread and rebound of liquid droplets upon impact on flat surfaces. *AIChE Journal, 43*, 2169–2179. https://doi.org/10.1002/aic.690430903. URL: https://aiche.onlinelibrary.wiley.com/doi/abs/10.1002/aic.690430903.

Mezhericher, M., Ladizhensky, I., & Etlin, I. (2017). Atomization of liquids by disintegrating thin liquid films using gas jets. *International Journal of Multiphase Flow, 88*, 99–115. https://doi.org/10.1016/j.ijmultiphaseflow.2016.07.015. URL: https://www.sciencedirect.com/science/article/pii/S0301932215301245.

Mezhericher, M., Nunes, J. K., Guzowski, J. J., & Stone, H. A. (2018). Aerosol-assisted synthesis of submicron particles at room temperature using ultra-fine liquid atomization. *Chemical Engineering Journal, 346*, 606–620. https://doi.org/10.1016/j.cej.2018.04.054. URL: https://www.sciencedirect.com/science/article/pii/S138589471830620X.

Mezhericher, M., Pan, Z., & Stone, H. A. (2025). Micron and submicron diameter spray droplet generation, 2025. *International Patent Application WO2025/019302A1*.

Mezhericher, M., Razorenov, N., Mazor, G., Ju, Y., & Stone, H. A. (2019). Submicron aerosols of liquid fuels: Method of production, experimental characterization and a semi-empirical model. *Applied Energy, 235*, 1651–1663. https://doi.org/10.1016/j.apenergy.2018.10.062. URL: https://www.sciencedirect.com/science/article/pii/S0306261918316313.

Mezhericher, M., Rieck, C., Razorenov, N., & Tsotsas, E. (2020). Ultrathin coating of particles in fluidized bed using submicron droplet aerosol. *Particuology, 53*, 23–29. https://doi.org/10.1016/j.partic.2020.03.005. URL: https://www.sciencedirect.com/science/article/pii/S167420012030047X.

Mezhericher, M., & Stone, H. A. (2022). Possible, impossible, and expected diameters and production rates of droplets in aerosols and sprays. *Physical Review Fluids, 7*, Article 063602. https://doi.org/10.1103/PhysRevFluids.7.063602. URL: https://link.aps.org/doi/10.1103/PhysRevFluids.7.063602.

Mugele, F., & Baret, J.-C. (2005). Electrowetting: From basics to applications. *Journal of Physics: Condensed Matter, 17*, R705–R774. https://doi.org/10.1088/0953-8984/17/28/R01

Paretsky, L., Theodore, L., Pfeffer, R., & Squires, A. M. (1971). Panel bed filters for simultaneous removal of fly ash and sulfur dioxide. *Journal of the Air Pollution Control Association, 21*, 204–209. https://doi.org/10.1080/00022470.1971.10469520. URL: .

Pendse, H., & Tien, C. (1982). General correlation of the initial collection efficiency of granular filter beds. *AIChE Journal, 28*, 677–686. https://doi.org/10.1002/aic.690280421. URL: https://aiche.onlinelibrary.wiley.com/doi/abs/10.1002/aic.690280421.

Peters, M. H., Fan, L.-S., & Sweeney, T. L. (1982). Simulation of particulate removal in gas-solid fluidized beds. *AIChE Journal, 28*, 39–49. https://doi.org/10.1002/aic.690280107. URL: https://aiche.onlinelibrary.wiley.com/doi/abs/10.1002/aic.690280107.

Pietsch, S., Peter, A., Wahl, P., Khinast, J., & Heinrich, S. (2019). Measurement of granule layer thickness in a spouted bed coating process via optical coherence tomography. *Powder Technology, 356*, 139–147. https://doi.org/10.1016/j.powtec.2019.08.022. URL: https://www.sciencedirect.com/science/article/pii/S0032591019306217.

Poozesh, S., Mezhericher, M., Pan, Z., Chaudhary, U., Manikwar, P., & Stone, H. A. (2024). Rapid room-temperature aerosol dehydration versus spray drying: A novel paradigm in biopharmaceutical drying technologies. *Journal of Pharmaceutical Sciences, 113*, 974–981. https://doi.org/10.1016/j.xphs.2023.10.003. URL:.

Qian, G.-H., Burdick, I. W., Pfeffer, R., Shaw, H., & Stevens, J. G. (2004). Soot removal from diesel engine exhaust using a rotating fluidized bed filter. *Advances in Environmental Research, 8*, 387–395. https://doi.org/10.1016/S1093-0191(02)00117-X. URL: https://www.sciencedirect.com/science/article/pii/S109301910200117X.

Quetzeri-Santiago, M., Castrejón-Pita, A., & Castrejon-Pita, R. (2019). The effect of surface roughness on the contact line and splashing dynamics of impacting droplets. *Scientific Reports, 9*. https://doi.org/10.1038/s41598-019-51490-5

Redón, R., Vázquez-Olmos, A., Mata-Zamora, M., Ordóñez-Medrano, A., Rivera-Torres, F., & Saniger, J. (2005). Contact angle studies on anodic porous alumina. *Journal of Colloid and Interface Science, 287*, 664–670. https://doi.org/10.1016/j.jcis.2005.02.036. URL: https://www.sciencedirect.com/science/article/pii/S0021979705001815.

Rieck, C., Bück, A., & Tsotsas, E. (2016). Monte Carlo modeling of fluidized bed coating and layering processes. *AIChE Journal, 62*, 2670–2680. https://doi.org/10.1002/aic.15237. URL: https://aiche.onlinelibrary.wiley.com/doi/abs/10.1002/aic.15237.

Rieck, C., Bück, A., & Tsotsas, E. (2020). Estimation of the dominant size enlargement mechanism in spray fluidized bed processes. *AIChE Journal, 66*, Article e16920. https://doi.org/10.1002/aic.16920. URL: https://aiche.onlinelibrary.wiley.com/doi/abs/10.1002/aic.16920.

Rieck, C., Hoffmann, T., Bück, A., Peglow, M., & Tsotsas, E. (2015). Influence of drying conditions on layer porosity in fluidized bed spray granulation. *Powder Technology, 272*, 120–131. https://doi.org/10.1016/j.powtec.2014.11.019. URL: https://www.sciencedirect.com/science/article/pii/S0032591014009176.

Sharma, G. S., Sugavaneswaran, M., Vijayalakshmi, U., & Prakash, R. (2019). Influence of $\gamma$-alumina coating on surface properties of direct metal laser sintered 316L stainless steel. *Ceramics International, 45*, 13456–13463. https://doi.org/10.1016/j.ceramint.2019.04.046. URL: https://www.sciencedirect.com/science/article/pii/S0272884219308673.

Sivakumar, D., Vankeswaram, S., Sakthikumar, R., & Raghunandan, B. (2015). Analysis on the atomization characteristics of aviation biofuel discharging from simplex swirl atomizer. *International Journal of Multiphase Flow, 72*, 88–96. https://doi.org/10.1016/j.ijmultiphaseflow.2015.02.009. URL: https://www.sciencedirect.com/science/article/pii/S0301932215000300.

Sondej, F., Bück, A., Koslowsky, K., Bachmann, P., Jacob, M., & Tsotsas, E. (2015). Investigation of coating layer morphology by micro-computed X-ray tomography. *Powder Technology, 273*, 165–175. https://doi.org/10.1016/j.powtec.2014.12.050. URL: https://www.sciencedirect.com/science/article/pii/S0032591014010328.

Sondej, F., Bück, A., & Tsotsas, E. (2016). Comparative analysis of the coating thickness on single particles using X-ray micro-computed tomography and confocal laser-scanning microscopy. *Powder Technology, 287*, 330–340. https://doi.org/10.1016/j.powtec.2015.09.039. URL: https://www.sciencedirect.com/science/article/pii/S0032591015300863.

Sondej, F., Peglow, M., Bück, A., & Tsotsas, E. (2018). Experimental investigation of the morphology of salt deposits from drying sessile droplets by white-light interferometry. *AIChE Journal, 64*, 2002–2016. https://doi.org/10.1002/aic.16085. URL: https://aiche.onlinelibrary.wiley.com/doi/abs/10.1002/aic.16085.

Teng, P., Tian, D., Fu, H., & Wang, S. (2020). Recent progress of electrowetting for droplet manipulation: From wetting to superwetting systems. *Materials Chemistry Frontiers, 4*, 140–154. https://doi.org/10.1039/C9QM00458K. URL:.

Terrazas-Velarde, K. (2010). *Monte carlo simulation of fluidized bed spray agglomeration*. Ph.D. Thesis. Otto von Guericke University Magdeburg.

Terrazas-Velarde, K., Peglow, M., & Tsotsas, E. (2009). Stochastic simulation of agglomerate formation in fluidized bed spray drying: A micro-scale approach. *Chemical Engineering Science, 64*, 2631–2643. https://doi.org/10.1016/j.ces.2009.02.041. URL: https://www.sciencedirect.com/science/article/pii/S000925090900147X.

Terrazas-Velarde, K., Peglow, M., & Tsotsas, E. (2011a). Kinetics of fluidized bed spray agglomeration for compact and porous particles. *Chemical Engineering Science, 66*, 1866–1878. https://doi.org/10.1016/j.ces.2011.01.037. URL: https://www.sciencedirect.com/science/article/pii/S0009250911000571.

Terrazas-Velarde, K., Peglow, M., & Tsotsas, E. (2011b). Investigation of the kinetics of fluidized bed spray agglomeration based on stochastic methods. *AIChE Journal, 57*, 3012–3026. https://doi.org/10.1002/aic.12506. URL: https://aiche.onlinelibrary.wiley.com/doi/abs/10.1002/aic.12506.

Tien, C. (1982). Aerosol filtration in granular media. *Chemical Engineering Communications, 17*, 361–382. https://doi.org/10.1080/00986448208911638. URL: .

Tsotsas, E. (2012). Influence of drying kinetics on particle formation: A personal perspective. *Drying Technology, 30*, 1167–1175. https://doi.org/10.1080/07373937.2012.685139. URL:.

Turton, R., Tardos, G. I., & Ennis, B. J. (1999). Fluidized bed coating and granulation. In W.-C. Yang (Ed.), *Fluidization, solids handling, and processing* (pp. 331–434). Westwood, NJ: William Andrew Publishing. https://doi.org/10.1016/B978-081551427-5.50008-9. URL: https://www.sciencedirect.com/science/article/pii/B9780815514275500089.

Ushiki, K., & Tien, C. (1984). Calculation of aerosol collection in fluidized filter beds. *AIChE Journal, 30*, 156–168. https://doi.org/10.1002/aic.690300122. URL: https://aiche.onlinelibrary.wiley.com/doi/abs/10.1002/aic.690300122.

Wan, L. S., & Lai, W. (1991). Factors affecting drug release from drug-coated granules prepared by fluidized-bed coating. *International Journal of Pharmaceutics, 72*, 163–174. https://doi.org/10.1016/0378-5173(91)90055-S. URL: https://www.sciencedirect.com/science/article/pii/037851739190055S.

Wenzel, R. N. (1936). Resistance of solid surfaces to wetting by water. *Industrial & Engineering Chemistry, 28*, 988–994. https://doi.org/10.1021/ie50320a024. URL:.

Werner, S. R., Jones, J. R., Paterson, A. H., Archer, R. H., & Pearce, D. L. (2007). Air-suspension particle coating in the food industry: Part I — State of the art. *Powder Technology, 171*, 25–33. https://doi.org/10.1016/j.powtec.2006.08.014. URL: https://www.sciencedirect.com/science/article/pii/S0032591006003470.

Zhang, J., Yao, S., Patel, H., & Fang, T. (2011). An experimental study on gasoline direct-injection spray and atomization characteristics of alcohol fuels and isooctane. *Atomization and Sprays, 21*, 363–374. https://doi.org/10.1615/AtomizSpr.2011003624

Zuo, T.-T., Walther, F., Ahmed, S., Rueß, R., Hertle, J., Mogwitz, B., Volz, K., & Janek, J. (2023). Formation of an artificial cathode-electrolyte interphase to suppress interfacial degradation of Ni-rich cathode active material with sulfide electrolytes for solid-state batteries. *ACS Energy Letters, 8*, 1322–1329. https://doi.org/10.1021/acsenergylett.2c02835. URL:.